Research Article

Late Oligocene-Miocene proto-Antarctic Circumpolar Current dynamics off the Wilkes Land margin, East Antarctica

Dimitris Evangelinos[a,*], Carlota Escutia[a], Johan Etourneau[a,b,c], Frida Hoem[d], Peter Bijl[d], Wilrieke Boterblom[d], Tina van de Flierdt[e], Luis Valero[f], José-Abel Flores[g], Francisco J. Rodriguez-Tovar[h], Francisco J. Jimenez-Espejo[a], Ariadna Salabarnada[a], Adrián López-Quirós[a]

[a] Instituto Andaluz de Ciencias de la Tierra, CSIC-Univ. de Granada, Av. de las Palmeras, 4, 18100 Armilla, Spain
[b] EPHE, PSL University, Paris, France
[c] UMR 5805 EPOC CNRS, University of Bordeaux, Bordeaux, France
[d] Palaeoecology, Institute of Environmental Biology, Faculty of Science, Laboratory of Palaeobotany and Palynology, Utrecht University, Budapestlann, 4, 3584, CD, Utrecht, the Netherlands
[e] Department of Earth Sciences and Engineering, South Kensington Campus, London SW7 2AZ, United Kingdom
[f] Département des Sciences de la Terre, Université de Genève, Rue des Maraîchers 13, 1205 Geneva, Switzerland
[g] Department of Geology, University of Salamanca, 37008 Salamanca, Spain
[h] Departamento de Estratigrafía y Paleontología, Facultad de Ciencias, Universidad de Granada, 18002 Granada, Spain

ARTICLE INFO

ABSTRACT

At present, the Southern Ocean plays an important role in the global climate system and in modern Antarctic ice sheet dynamics. Past Southern Ocean configurations are however poorly understood. This information is yet important as it may provide important insights into the climate system and past ice-sheet behavior under warmer than present day climates. Here we study Southern Ocean dynamics during the Oligocene and Miocene when reconstructed atmospheric CO_2 concentrations were similar to those expected during this century. We reconstruct snapshots of late Oligocene to earliest Miocene (~24.2–23 Ma) paleoceanographic conditions in the East Antarctic Wilkes Land abyssal plain. For this, we combine marine sedimentological, geochemical (X-ray fluorescence, TEX_{86}), palynological and isotopic (ε_{Nd}) records from ocean sediments recovered at Deep Sea Drilling Project (DSDP) Site 269. Overall, we find that sediments, delivered to the site by gravity flows and hemipelagic settling during glacial-interglacial cycles, were persistently reworked by a proto-Circumpolar Deep Water (CDW) with varying strengths that result from climatically controlled frontal system migrations. Just prior to 24 Ma, terrigenous input of predominantly fine-grained sediments deposited under weak proto-CDW intensities and poorly ventilated bottom conditions dominates. In comparison, 24 Ma marks the start of episodic events of enhanced proto-CDW current velocities, associated with coarse-grained deposits and better-ventilated bottom conditions. In particular, the dominance of P-cyst and low Calcium (Ca) in the sediments between ~ 24.2 Ma and 23.6 Ma indicate the presence of an active open ocean upwelling associated with high nutrient conditions. This is supported by TEX_{86}-derived sea surface temperature (SST) data pointing to cool ocean conditions. From ~ 23.6 to 23.2 Ma, our records reveal an enrichment of Ca in the sediments related to increased calcareous microfossil preservation, high amounts of G-cysts and increasing TEX_{86}-SSTs. This implies warmer water masses reaching the Antarctic margin as the polar front migrated southward. Together with the radiogenic Nd isotope data indicating modern-like CDW values, our records suggest a prominent poleward expansion of proto-CDW over our study site and reduced AABW formation during the latest Oligocene (i.e. ~23.2 Ma ago). Our findings support the notion of a fundamentally different Southern Ocean, with a weaker proto-ACC than present during the late Oligocene and the earliest Miocene.

* Corresponding author.
  E-mail address: dimevangelinos@correo.ugr.es (D. Evangelinos).

1. Introduction

The Antarctic Circumpolar Current (ACC) is the Earth's strongest ocean current (137–162 sverdrup (Sv)) flowing eastward along a 20,000 km pathway around Antarctica (Rintoul et al., 2001; Sokolov and Rintoul, 2009). Owing to the absence of land barriers, the ACC is the only ocean current connecting the Pacific, the Atlantic and the Indian oceans, and consequently influences the entire global ocean circulation (Rintoul, 2018). The ACC pathway is constrained by ocean gateways (i.e. Drake Passage) and the bathymetry of the Southern Ocean. Its strength is mainly controlled by the seafloor topography (Olbers et al., 2004), and the position and intensity of the Southern Westerly Winds (SWW) (Thompson and Solomon, 2002; Aoki et al., 2005; Toggweiler and Russell, 2008; Rignot et al., 2019). At present, the vigorous zonal flow of the ACC prevents the intrusion of warm waters from lower latitudes to penetrate the Antarctic margin and, together with sea-ice presence, contributes to maintain the cold and arid glacial state of Antarctica (e.g., Olbers et al., 2004; Ferrari et al., 2014). The deep layers of the ACC are occupied by a relatively warm and saline water mass, the Circumpolar Deep Water (CDW) (Orsi et al., 1995). Recently, an increasing incursion of CDW into the continental margins has been shown to favor melting and thinning of the Antarctic ice shelves through basal melting (Pritchard et al., 2012; Liu et al., 2015; Nakayama et al., 2018; Rignot et al., 2019). Despite its importance for the Antarctic and the global climate, little is known about the onset and past dynamics of the ACC, as well as its linkages with the Antarctic Ice sheet (AIS) dynamics. This knowledge is especially relevant from past times when climatic conditions were close to the modern and future ones in terms of warmth and atmospheric CO_2 concentration.

One of these times was the late Oligocene (i.e., ~24.5 Ma), when the reconstructed atmospheric CO_2 concentrations dropped below 600 ppm (600–400 ppm) (Zhang et al., 2013). These values are similar to the modern and projected atmospheric CO_2 concentrations within this century (IPCC, 2013; Meredith et al., 2019). Foster and Rohling (2013) argued that the global ice volume is supposedly less sensitive to CO_2 fluctuations between 600 and 400 ppm. In contrast, benthic foraminiferal oxygen isotope records (e.g., Liebrand et al., 2017) suggest highly fluctuating ice volumes at this time. The drop in CO_2 concentration in the late Oligocene (~24.5 Ma) likely led to climate cooling and ice sheet advance across the Antarctic continental shelves, connecting large areas of marine-based ice with the ocean (Pekar and Christie-Blick, 2008; Levy et al., 2019). Ice-proximal geological records (Barrett, 1975; Naish et al., 2008; Kulhanek et al., 2019; Levy et al., 2019) and seismic data (Anderson and Bartek, 1992; Sorlien et al., 2007) provide direct evidence for a major expansion of marine ice sheets across the Ross Sea continental shelf between 24.5 and 24 Ma. However, the oceanographic and climatic conditions leading to the maximum growth of the ice sheet remain poorly known.

The global deep-sea benthic $\delta^{18}O$ records maximum expansion of the AIS between 23.2 and 23 Ma (Zachos et al., 2001; Beddow et al., 2016; Liebrand et al., 2017). However, deep-sea benthic $\delta^{18}O$ records reflect a combination of ice-volume and bottom water temperature and their location (low to mid-latitude versus Antarctic proximal records) determines the different water masses influencing the record and thus masking information from the Antarctic glaciation (e.g., Pekar et al., 2006). Thus, most of the ice volume estimates based on deep-sea benthic $\delta^{18}O$ records should be taken with caution. Variations in the Southern Ocean circulation and ocean heat transport across the Antarctic continental margin driven by obliquity forcing have been suggested to play a significant role on ice sheet sensitivity during the late Oligocene and Miocene (Salabarnada et al., 2018; Sangiorgi et al., 2018; Levy et al., 2019). This is especially true in times when ice sheets extended into the marine environments (e.g., Jovane et al., 2019; Levy et al., 2019). Sedimentary archives strategically located along latitudinal transects across the main ACC pathway and at the vicinity of the Antarctic ice sheet are however needed to provide direct links between

changes in the ocean circulation and ice sheet dynamics (Escutia et al., 2019).

Sedimentary records across the Tasman Gateway (Pfuhl and McCave, 2005) and from the South Pacific (Lyle et al., 2007) document a shift to higher velocity bottom currents between 25 and 23 Ma. This shift has been interpreted to result from the onset of a strong, deep-reaching ACC during the late Oligocene. However, recent comparisons between the dinocysts preserved in sediments from the Integrated Ocean Drilling Program (IODP) Site U1356 off the East Antarctic Wilkes Land margin and strata from Tasmania and south of New Zealand indicate a weaker than present day ACC, at least until the middle Miocene (Bijl et al., 2018b). Oligocene and Miocene paleoceanographic reconstructions off the Wilkes Land margin based on sedimentological data (Salabarnada et al., 2018), dinoflagellate biogeography (Bijl et al., 2018a, 2018b; Sangiorgi et al., 2018) and temperature reconstructions (Hartman et al., 2018) suggest a different oceanographic configuration from that of today in this part of the Southern Ocean. These authors report from multiple lines of evidence warm-temperate sea surface temperatures (SST), limited sea ice expansion and reduced formation of Antarctic bottom waters, linked to a weaker oceanic frontal system, which allowed the intrusion of warmer waters from low latitudes towards the Antarctic margin. These data are consistent with Oligocene numerical simulations, which show weaker global overturning and gyre circulation because of weaker SWW (Herold et al., 2012). In addition, modeling results indicate a limited throughflow of the ACC due to the Australasian paleogeography during the Oligocene (Hill et al., 2013).

To decipher the characteristics and dynamics of the ACC and CDW that can then be related to East Antarctic Ice Sheet (EAIS) behavior off Wilkes-Adélie Land during the late Oligocene-Miocene, we report new data from a sediment record recovered by the Deep Sea Drilling Project (DSDP) Leg 28 at Site 269. This site was drilled on the Wilkes Land abyssal plain (Hayes et al., 1975) along the main pathway of the ACC. We focus on the study of the late Oligocene to earliest Miocene (~24.2–23 Ma) record. This record is partly compromised by debris flows at IODP Site U1356, located on the continental rise (Escutia et al., 2011), ~280 km landward from Site 269, and is missing in most sedimentary archives around the rest of Antarctica. Because of discontinuous drilling at Site 269, we investigate snapshots of the late Oligocene and early Miocene. Sediment, palynological, geochemical and isotopic data are used to describe and characterise the main changes in sedimentation related to proto-CDW dynamics. The findings at DSDP Site 269 are then compared to results from IODP Site U1356 (Escutia et al., 2011, 2014; Salabarnada et al., 2018) (Fig. 1). This latitudinal comparison provides important insights into changes in proto-ACC dynamics that can in turn be related to the evolution of the ice sheet in this region of the East Antarctic margin.

2. Site description and oceanographic setting

DSDP Leg 28 Site 269 is located on the abyssal plain off the Wilkes Land (61°40.57′S, 140°04.21′E, 4282 m water depth) (Hayes et al., 1975) (Fig. 1). Two holes were discontinuously drilled at this site. Our study focuses on Hole 269A, specifically the interval between 655 and 956 m below sea floor (mbsf) (cores 7R to 13R). Recovered sediments were interpreted shipboard to be mostly turbidites, but evidence of winnowing by bottom currents was also documented (Hayes et al., 1975). Facies were identified within the frame of the DSDP Leg 28 expedition mainly based on the lithology, bioturbation and bed contacts (Piper and Brisco, 1975).

At present, Site 269 is located between the modern southern branch of the Polar Front (PF) and the northern branch of the Southern ACC Front (SACCF). In comparison, Site U1356 (63°18.6138′S, 135°59.9376′E, 3992 m water depth) lies south of the SACCF, near the Antarctic Divergence (Sokolov and Rintoul, 2002) (Fig. 1). Both sites are today covered by the Adélie Land Bottom Water (ALBW) (Rintoul, 1998), which forms in winter time along the Adélie-Wilkes Land Coast
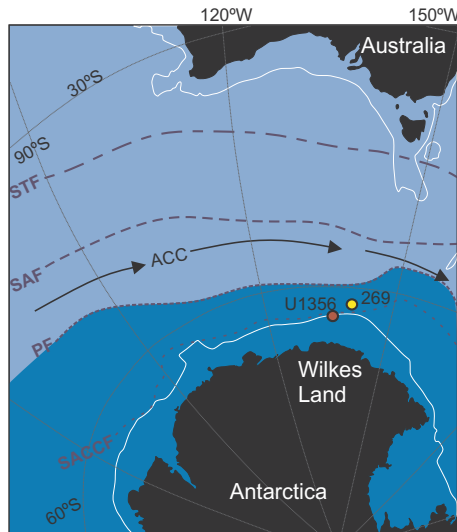
Fig. 1. Oceanic frontal system between Antarctica and Australia. Dark Blue dashed lines schematically represent oceanic fronts today (Sokolov and Rintoul, 2009). Polar water south of the PF are shaded in darker blue. Map derived from Gplates software (Müller et al., 2018). Site 269 is marked with yellow symbol and Site U1356 is marked with red symbol. White lines indicates the continental lithosphere boundary. Black arrows show the pathway of the ACC today (Rintoul et al., 2001). STF: Subtropical front, SAF: Subantarctic front, PF: Polar Front, SAACF: Southern ACC front, ACC: Antarctic Circumpolar Current. (For interpretation of the references to colour in this figure legend, the reader is referred to the web version of this article.)

(Orsi et al., 1995). Our reconstruction of the paleoposition of Site 269 and Site U1356 is adapted from G-plates geodynamic modeling (http://www.gplates.org; Müller et al., 2018), and uses the plate circuit of Seton et al. (2012). It shows that Site 269 has migrated south since the Oligocene but remained located at ~60°S between the late Oligocene-early Miocene, while the paleolatitude of Site U1356 was around 62°S. Geological evidence derived from the analysis of microfossil assemblages from sedimentary records around Antarctica suggest that the proto-Polar Front (PF) was situated close to 60°S between the late Oligocene-early Miocene (Nelson and Cooke, 2001; Cooke et al., 2002).

3. Revising the initial age model

We established a new age model based on the integration of new magnetostratigraphic data, dinocyst and calcareous nannofossil biostratigraphy, calibrated using the GTS 2012 Astronomic Age Model (Gradstein et al., 2012) (Figs. 2; S1; S2 and Tables S1; S2). The presence of *Operculodinium janduchenei* in the sediment between ±753–955 (mbsf) (Cores 9R 3 W to 13R) is assigned to the lower Southern Ocean Dinocyst Zone (SODZ) SODZ8 (Bijl et al., 2018a). This suggests that the bottom of Hole 269A cannot be older than late Oligocene (24.2 Ma). Moreover, the last occurrence of *Operculodinium janduchenei* between 753.27 and 752.32 mbsf (9R 3 W 125–129 cm - 9R 3 W 30–33 cm) marks the boundary between dinocysts zones SODZ8 and SODZ9. This boundary is calibrated to 23.6 Ma at U1356 (Bijl et al., 2018a) and is correlated to the reversed polarity found at the bottom of chron C6C (C6Cr). This is corroborated by the presence of *Cyclicargolithus abisectus* at 752.9 mbsf indicating that this interval corresponds to the zone NP 25 (Martini, 1971), which implies a latest Oligocene age. The latter however, must be taken with caution given the scarce amount of calcareous nannofossils, as well as the absence of other conventional markers. The presence of *Impagidinium aculeatum* at 658.82 mbsf (7R 4 W 30–34 cm) is assigned to the mid- of SODZ10 or older (~23 Ma) (Bijl et al., 2018a). This is correlated with the normal polarity of the geomagnetic chron C6n.2n suggesting also an age of 23 Ma. In addition,
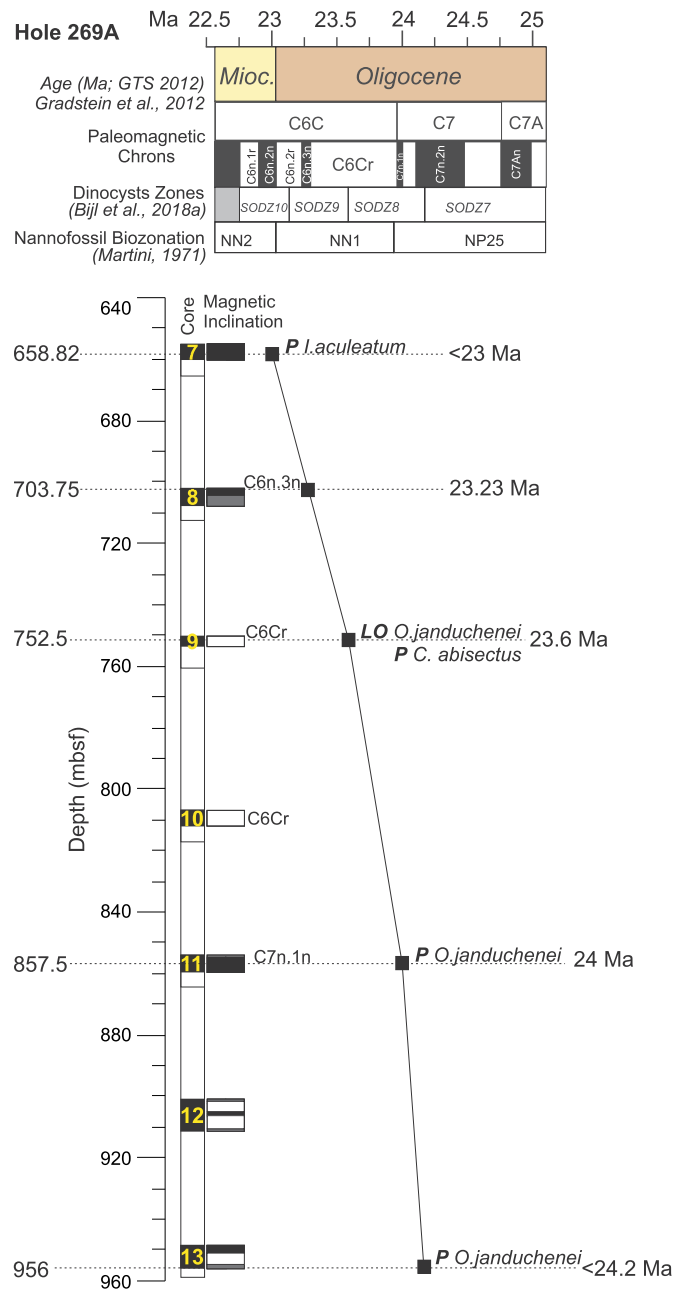

Fig. 2. Age model for Deep Sea Drilling Project Hole 269A based on magnetostratigraphy constrained by dinocyst and calcareous nannofossil biostratigraphy. **LO:** Last Occurrence. **P:** Presence. Age model has been calibrated to GTS2012 of Gradstein et al. (2012).

based on the biostratigraphic datums we assigned the paleomagnetic reversal at ~857.5 mbsf to chron C7n.1n (24 Ma) and at ~703 mbsf to chron C6n.3n (23.23 Ma). Our updated age model suggests an age range for the studied interval from ~24.2 to ~23 Ma (Fig. 2). Initial shipboard data had dated this interval to be of middle Eocene to early Oligocene age (Hayes et al., 1975). We acknowledge that the age model still has large uncertainties due to discontinuous coring, incomplete recovery and the low preservation of microfossils. However, the integration of the well-established Southern Ocean Oligocene-Miocene dinocyst stratigraphy, which was developed at the nearby Site U1356 along with the good correspondence with the magnetostratigraphic data allow us to be relatively confident in our age model.
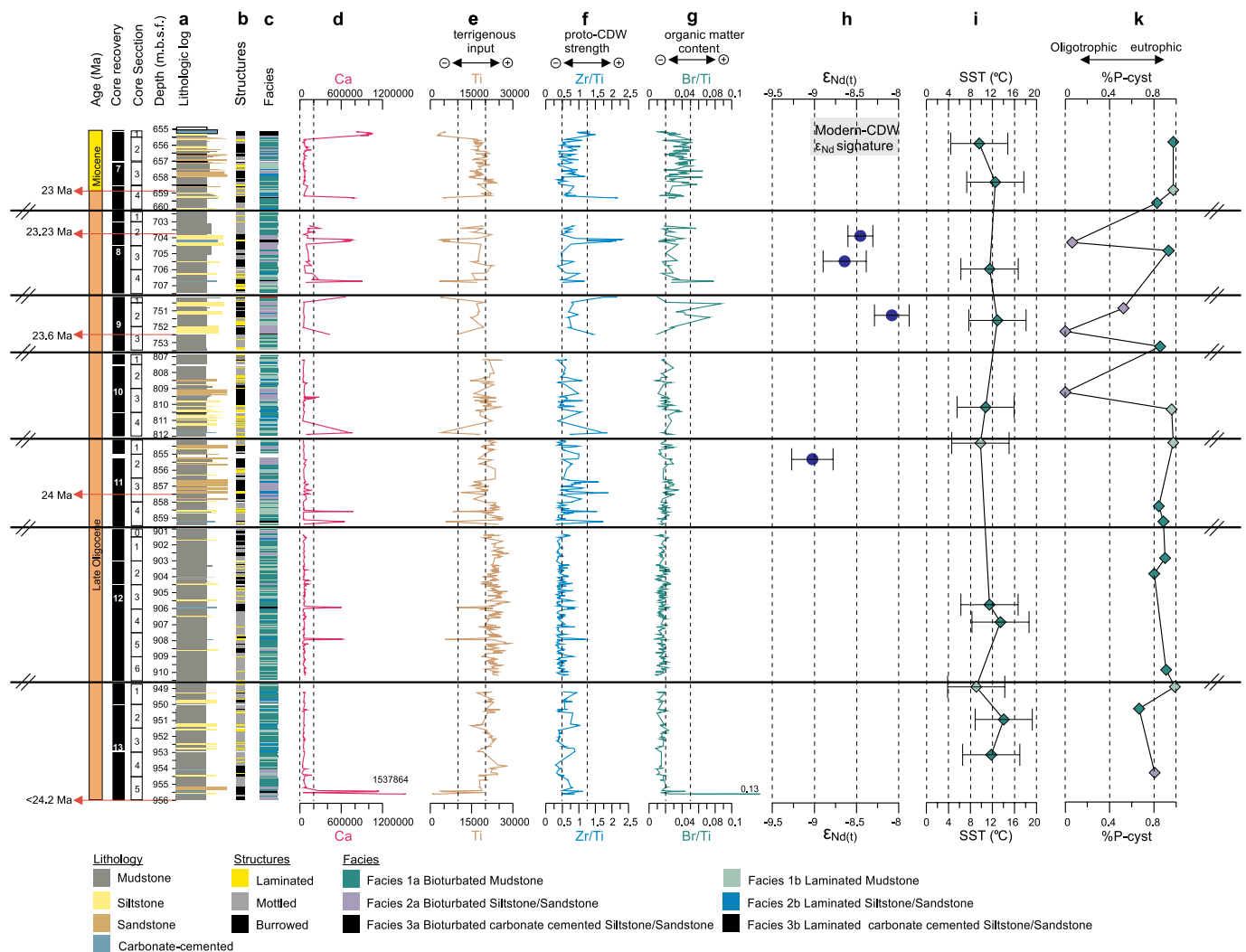
Fig. 3. Sedimentological, paleontological and geochemical (XRF scanning data and $\varepsilon_{Nd(t)}$) data of DSDP Hole 269A, all plotted versus depth **a:** Graphic lithological log, **b:** sedimentary structures (see legend), **c:** main facies distribution (see legend), **d:** total Ca counts, **e:** total Ti counts, **f:** Zr/Ti ratios, **g:** Br/Ti ratios, **h:** $\varepsilon_{Nd(t)}$, **i:** TEX$_{86}$-derived sea surface temperature (SST) **k:** %P-cyst = P-cyst/(P-cyst + G-cyst). Colors of TEX$_{86}$-derived SST and %P-cyst values reflect the sedimentary facies. Note core gaps between the cores were removed from the plot (gaps indicated with //).

4. Methods

4.1. Facies analysis

A detailed facies analysis was performed on sediment from Hole 269A to determine depositional processes and aid paleoenvironmental reconstructions. We conducted a detailed description of the cores using standard sedimentological techniques (i.e., lithological characterization, contacts, sedimentary structures and textures) in order to produce the lithostratigraphic log in Fig. 3 and Supplementary Fig. 3. Visual descriptions were aided by high-resolution digital images obtained on the archive halves using a Nikon 60 mm camera lens mounted on a custom-built line scanner at the Coast Gulf Repository (CGR), in College Station (Texas, USA). High-resolution images were also used for ichnological analysis (i.e., type and degree of bioturbation) performed to characterise the paleoenvironmental conditions prevailing in the seafloor. Ichnological analysis was based on the digital treatment of the high-resolution images following previous researches (Dorador and Rodríguez-Tovar, 2014; Dorador et al., 2014a; Dorador et al., 2014b; Rodríguez-Tovar and Dorador, 2015; Dorador and Rodríguez-Tovar, 2018). It was conducted at the Department of Stratigraphy and Paleontology at the University of Granada (Spain). Further

characterization of the biogenic and terrigenous material within each of the lithofacies defined was achieved by: 1) Bulk grain-size analyses that was performed at EPOC (Environnements et Paléoenvironnements Océaniques et Continentaux) (Bordeaux, France). In total 44 sediment samples (dried overnight in an oven at 40 °C) were measured in a laser microgranulometer Malvern mastersizer hydro 2000G with automatic samples (0.020 to 2000 μm). 2) Wet sieving and High-Resolution Scanning Electron Microscope (HR-SEM) analysis conducted at the Instituto Andaluz de Ciencias de la Tierra, (CSIC, Spain) and at the Centro de Instrumentación Científica (University of Granada, Spain), respectively. Moreover, continuous measurements of magnetic susceptibility (MS) were taken from the archive half sections of the core. For this, the core sections were left out of the refrigerator overnight to acquire a room temperature before scanning. MS measurements were taken every 2 cm using a Bartington MS2 mounted in a Geotek Multi-Sensor Core Logger (MSCL) at the GCR. Core void measurements were removed from the data set.

4.2. Major and trace element content

The elemental composition of sediments derived from X-Ray Fluorescence (XRF) core scanners has been used as an indicator of past

climate changes in proximal and distal records from the Antarctic margin. For example, titanium (Ti), aluminium (Al), iron (Fe) versus calcium (Ca) have been interpreted to show changes between terrigenous and biogenic $CaCO_3$ deposition (e.g., Grützner et al., 2005; Hepp et al., 2006; Escutia et al., 2009; Salabarnada et al., 2018). In addition, zirconium-based proxies (e.g. Zr/Ti ratios) have previously been used as an indicator of semiquantitative assessment of bottom current velocities in Oligocene sediments from Site U1356 off Wilkes Land (Salabarnada et al., 2018). This is based on the relative enrichment of heavy minerals such as zircon over less dense minerals (e.g., aluminosilicates) that result from hydrodynamic winnowing and sorting of heavy minerals (e.g., Bahr et al., 2014). Bromine (Br)/Ti ratios have been used as indicator of organic matter in the sediments (Bahr et al., 2014; Salabarnada et al., 2018). The Br content is associated to total organic carbon (TOC) concentration in the sediments (Seki et al., 2019), and TOC is mainly related to changes in productivity (organic carbon flux in the sediments) and/or changes in the redox state of the sediment (e.g., Jimenez-Espejo et al., 2007). Br is not biased by lithological changes (i.e. mudstones/sandstones), but is affected by organic matter degradation (Bahr et al., 2014).

XRF core scanning measurements were conducted at 10 kV and 30 kV on the archive split sections from Cores 7R to 13R using an Avaatech XRF core scanner at the GCR. The surface of core sections was cleaned carefully for any gypsum and salts, which might have precipitated and then adjusted manually to form an even surface. A 4 μm thick ultralene plastic film was used to cover the core surface in order to avoid contamination while scanning. Due to the presence of cracks in many core sections, spot measurements were taken rather than scan the section continuously.

To decipher the different processes influencing the geochemical composition of the sediment, we conducted a Principle Component Analysis (PCA). We used the PAST version 2.10 software package (Hammer et al., 2001) following the data pre-treatment in Bahr et al. (2014), including normalization of the data to reduce the signal artefacts related to changes in lithology. For the PCA, we only selected and show elements with a robust signal quality, i.e., Al, Si, K, Ca, Ti, Fe, Ba, Br, Rb, Sr, and Zr. In this study we report on the following elements and elemental ratios Ca, Ti, Zr/Ti ratios and Br/Ti ratios.

4.3. Neodymium isotopes

Neodymium (Nd) is delivered to the ocean through the weathering of continental crust, and by exchange with sediment on the continental margin (known as boundary exchange; e.g., Frank, 2002, Wilson et al., 2013). Consequently, water masses forming in different geological basins will be isotopically distinct. Because of its short oceanic residence time in the ocean (~400–1000 yr) relative to oceanic mixing (1500 yr) (Tachikawa et al., 2003) records of Nd isotopes allow us to reconstruct past ocean circulation and changes in the weathering inputs. Neodymium isotopes in fossil fish debris are a robust tool to reconstruct changes in ocean circulation by identifying distinct water masses (e.g. Goldstein and Hemming, 2003; Martin and Scher, 2004; van de Flierdt et al., 2016). Neodymium is incorporated into the fish teeth during the fossilization processes at the sediment-water interface and reflects the isotopic composition of seawater in contact with the seafloor at the time of fish tooth deposition, remineralisation and burial (Shaw and Wasserburg, 1985). Neodymium isotope ratios in fossil fish teeth are considered to be resistant to changes in post-burial alteration (Martin and Scher, 2004; Scher et al., 2011). Neodymium isotope ratios ($^{143}Nd/^{144}Nd$) are expressed as ε_{Nd}, which denotes the deviation of a measured $^{143}Nd/^{144}Nd$ ratio from the chondritic uniform reservoir in parts per 10,000 (DePaolo, 1976; Jacobsen and Wasserburg, 1980).

Fish debris was handpicked from the >63 μm sediment fractions that were prepared by wet sieving. Four samples were prepared for fish-tooth and bone debris Nd isotope analyses in the MAGIC laboratories at Imperial College London following the sample preparation detailed in

supplementary materials. In addition, to account for a potential influence of the detrital sediment towards the Nd isotope composition of pore waters or overlying bottom water, we also measured the Nd isotope compositions of two detrital sediment samples. Sample preparation for these analyses was conducted in the MAGIC laboratories at Imperial College London as detailed in supplementary materials. The detrital samples were processed using the same ion chromatography as the fish debris.

Neodymium isotope ratios for fish debris and detrital sediment samples were determined on a Nu Plasma multiple collector inductively coupled plasma mass spectrometer (MC-ICP-MS) at Imperial College London, operated in static mode. Instrumental mass bias was corrected using the $^{146}Nd/^{144}Nd$ ratio of 0.7219. A JNdi-1 isotope standard was run after every sample and all reported $^{143}Nd/^{144}Nd$ ratios are corrected to a JNd_i value of 0.512115 (Tanaka et al., 2000) using bracketing standards. External reproducibility was monitored using the JNd_i standards, and accuracy was confirmed by measuring USGS BCR-2 rock standards, which yielded average $^{143}Nd/^{144}Nd$ ratios in agreement with the published BCR-2 $^{143}Nd/^{144}Nd$ ratio of 0.512638 ± 0.000015 (Weis et al., 2006).

To correct for the decay of ^{147}Sm to ^{144}Nd within the fish teeth over time we used Sm and Nd concentrations obtained from two samples, which were in good agreement with $^{147}Sm/^{144}Nd$ ratios reported from fossil fish teeth in other marine sedimentary records (e.g., Martin and Scher, 2006; Moiroud et al., 2013; Huck et al., 2017; Wright et al., 2018). When no values available, an average of 0.1286 from the measured samples was applied to calculate $\varepsilon_{Nd(t)}$ values. The $^{147}Sm/^{144}Nd$ ratios yielded Nd isotope corrections of 0.19 to 0.21 ε_{Nd} units; (t) denotes samples have been corrected for in situ decay of ^{147}Sm.

4.4. TEX$_{86}$

The TetraEther indeX of 86 carbon atoms (TEX$_{86}$) is a proxy for sea surface temperature (SST). The TEX$_{86}$ paleothermometer employs the temperature-dependent relative abundance of a suite of thaumarchaeotal membrane lipids; glycerol dibiphytanyl glycerol tetraethers (GDGTs) (Schouten et al., 2002, 2013). In short, this method involves lipid extraction from powdered and freeze-dried sediments using accelerated solvent extraction. Lipid extracts were separated into an apolar, ketone and polar fraction by Al_2O_3 column chromatography using hexane:DCM (9:1), hexane:DCM (1:1) and DCM:MeOH (1:1) as respective eluents. 99 ng of a synthetic C_{46} (mass-to-charge ratio, m/z = 744) GDGT standard was added to the polar fraction, which then was dissolved in hexane:isopropanol (99:1, v/v) to a concentration of ~3 mg ml^{-1} and filtered over a 0.45-μm polytetrafluoroethylene filter. The dissolved polar fractions were injected and analysed by high-performance liquid chromatography–mass spectrometry (HPLC–MS), using the double column technique for improved separation of co-eluting compounds (Hopmans et al., 2015). GDGT peaks in the HPLC chromatograms were integrated using ChemStation software. Several calibrations have been proposed to translate TEX$_{86}$ into SST. We employ the TEX$_{86}$ linear calibration (SST = 81.5 × TEX$_{86}$–26.6 with a calibration error of ± 5.2∘C) by Kim et al. (2010), to enable adequate comparison to existing data, and following elaborate discussions in Hartman et al. (2018). We provide the GDGT peak areas and R-script in the online supplementary materials.

Before interpreting the TEX$_{86}$ results into SST reconstructions samples with overprint, which may affect the reliability of the SST proxy, must be discarded. Terrestrial GDGT input has been reconstructed using the branched and isoprenoid tetraether (BIT) index (Hopmans et al., 2004) as a proxy. Samples with a high BIT index may be biased by soil- and river-derived GDGTs (Hopmans et al., 2004), although the high BIT index may also stem from a decrease in marine crenarchaeol production, as the BIT index is a closed sum between terrestrial GDGTs and the exclusively marine crenachaeol. Several indices for a potential biased source of GDGTs was investigated and

outliers discarded. Namely, methane index (Zhang et al., 2011), flagging overprint by sedimentary methanogenic activity, GDGT-2/GDGT-3 ratio (Taylor et al., 2013), potentially signaling overprint by archaeal communities dwelling deeper into the water column, GDGT-0/Crenarchaeol ratio (Blaga et al., 2009; Damsté et al., 2009; Taylor et al., 2013), flagging overprint by in situ production of isoprenoidal GDGTs in lakes and rivers, and ring index (Zhang et al., 2016), which assesses an overall pelagic character for the different GDGTs within the TEX_{86} index. High-latitude TEX_{86} SST reconstructions might be skewed towards summer temperatures (Schouten et al., 2013; Ho et al., 2014; Hartman et al., 2018).) and potentially incorporate a subsurface signal (0–200 mbsl) (Hernández-Sánchez et al., 2014; Ho and Laepple, 2015). However, there is a general agreement that TEX_{86} captures the relative SST trend (Richey and Tierney, 2016).

4.5. Palynology – Dinoflagellate cyst paleoenvironment reconstruction

In total 19 sediment samples (~15 g) were processed for palynology and counted at Utrecht University using standard palynological processing and analytical procedures previously described by Bijl et al. (2013, 2018b). Modern dinoflagellate (unicellular planktonic protists) distribution are sensitive to small changes in nutrient availability, SST, salinity, bottom water oxygen, primary productivity and sea-ice cover (Dale, 1996; Prebble et al., 2013; Zonneveld et al., 2013). Approximately 13–16% produce an organic-walled cyst, dinocysts, that can preserve in the fossil record (Head, 1996). Assuming the habitat affinities and feeding strategies of most dinoflagellates can be extrapolated to the fossil assemblages, we can utilize 'deep-time' dinocysts assemblages as a paleoceanographic proxy (Sluijs et al., 2005; Bijl et al., 2013; Crouch et al., 2014). In the Southern Ocean, protoperidinioid (P) cysts originate from hetrotrophic dinoflagellates and proliferate under increased nutrient conditions, while gonyaulacoid (G) cysts originate from autotrophic or mixotrophix dinoflagellates and reflect oligotrophic conditions (Esper and Zonneveld, 2002). Thus, the relative P/G-cyst ratio can indicate glacial/interglacial variability and ocean frontal movement migrations. Today, the surface sediments at Site 269A consists almost exclusively of P-cysts, specifically the sea-ice affiliated species Selenopemphix antarctica (Prebble et al., 2013).

5. Results

5.1. Sedimentation at Hole 269A

Sediment from Hole 269A from 655 to 956 mbsf consists of alternations between bioturbated and laminated intervals of terrigenous-rich sediment (Figs. 3a, b, 4 and S3). Textural analyses show a low clay content (4 to 20%), a high silt fraction (40 to 80%) and a sand content between <5 and 60% (Fig. S3). Microfossil preservation is generally low throughout the study interval. Higher preservation of calcareous microfossils was found in the carbonate-cemented beds (Figs. 3a and 5) and within the sediments between 753.5 and 702.5 mbsf (~23.6 to 23.23 Ma) (Fig. S4). The higher calcareous carbonate preservation is depicted in Ca peaks in Fig. 3d. Higher preservation of diatoms is also observed in the carbonate-cemented facies (Fig. 5) and in Core 7 (660–655.5 mbsf) (~23 Ma).

The main observed differences within the bioturbated and laminated intervals are the variations in the silt/sand content, ichnological features, including amount of bioturbation, and carbonate content (carbonate-cemented intervals). Based on this, we differentiate the following sedimentary facies (Figs. 3c and 4): (1) Bioturbated silty claystones to clayey siltstones (Bioturbated mudstone; F1a), bioturbated siltstones to sandy siltstones (F2a), and bioturbated carbonate-cemented facies (F3a). (2) Laminated silty claystones to clayey siltstones (Laminated mudstone; F1b), laminated siltstones to sandy siltstones (F2b), and laminated carbonate-cemented facies (F3b).

Bioturbated facies (F1a, F2a and F3a; Figs. 3c, 4 and 5) generally

exhibit a structureless and/or mottled texture. Bioturbation varies from low, dominated by *Chondrites* and *Phycosiphon,* to high with abundant and diverse trace fossils, including *Planolites, Thalassinoides, Nereites, Zoophycos* and likely *Scolicia* (Fig. 4). The occurrence of coarser bioturbated facies (F2a) becomes more frequent up-section starting at 858 mbsf, but is also present in the lowermost part of the site at ~955.3 mbsf (Fig. 3c).

Laminated facies (F1b, F2b and F3b; Figs. 3c, 4 and 5) are characterized by faint and/or distinct sub-mm to mm silty-sandy laminations. Laminated intervals can contain a single or a group of laminae with various sedimentary structures, including continuous and discontinuous planar, wavy, lenticular, ripple and cross laminations (e.g., Fig. 4a). Small soft-sedimentary deformation structures such as convoluted, ball and pillow structures are often observed within the laminations (Fig. 4k). Scarce traces of *Chondrites* may be present.

Despite the diagenetic processes associated with the bioturbated and laminated carbonate-cemented facies (F3a, F3b), thin section analyses integrated with HR-SEM images show preservation of microfossils in both facies, including silicified planktonic foraminifers and diatoms (Figs. 5f-h). This observation is noteworthy since the sediments of the study sections were considered almost barren in microfossil (Hayes et al., 1975). The presence of benthic foraminifera with siliceous test suggests diagenetic dissolution and confirms the biogenic origin of these carbonates (Fig. 5). HR-SEM images reveal that the contact between F3b and F3a is sharp and erosive and inverse grading characterizes F3b (Fig. 5e). In total thirteen carbonate-cemented beds were observed, with the thickest ones at 704.2 mbsf and at 655.3 mbsf (e.g., Fig. 3c and d).

The intercalation of bioturbated and laminated facies is characterized by both gradational and sharp contacts. More than 90 sharp contacts were identified (Fig. S3). A common ichnological feature that appears associated with at the sharp contact between the coarse and the fine-grained facies is the presence of pseudo-borings, characterized by well-defined shapes, undeformed, with sharp contacts, infilled with different material to the host sediment (Figs. 4 d-f).

5.2. Geochemistry at Hole 269A

Down-core variations of Ca content clearly track the 13 carbonate-cemented beds (Fig. 3d). In these beds, the dissolution of calcareous microfossils results in carbonate cementation/re-precipitation, as shown by the HR-SEM analyses (Fig. 5h). Additionally, we observe an interval of increased Ca values within the non-carbonate-cemented sediments between 706.8 and 703.28 mbsf (~23.23 Ma) (Fig. 3d). This increase is also associated with the preservation, even if scarce, of calcareous microfossils (i.e., planktonic, benthic foraminifers and calcareous nannofossils, Fig. S4).

In comparison, Ti variations show negative excursions in the carbonate-cemented facies (Fig. 3e). Ti decreases after 858 mbsf (~24 Ma), and more pronounced between 752.5 and 655 mbsf (~23.6 to 23 Ma) (Fig. 3e).

A principal component analyses (PCA) yielded one major principal component ($PC1_{TOT}$) that explains 63.8% of the total variance in the XRF data (Table S4). $PC1_{TOT}$ is characterized by negative loadings for Ca and positive loading for all the other elements (Al, Si, K, Ti, Fe, Br, Ba, Sr, Zr) (Fig. 6a). Prominent negative excursions in $PC1_{TOT}$, are associated with the carbonate-cemented beds. In addition, $PC1_{TOT}$ decreases after 752.5 mbsf (~23.6 Ma) (Fig. S5).

Because of the distinct lithological/geochemical characteristics of carbonate-cemented beds compared to the rest of the sediments in our record, we ran another PCA, excluding the carbonate-cemented sediment. The first PC, named PC1 describes the 34.7% of the total variance, with main negative loadings for Zr and Ca and in lesser degree Sr, Br and Si and positive loading for all the other detrital elements (Al, Si, K, Ti, Fe, Ba, Rb) (Table S3; Fig. 6b). This pattern suggests accumulation of heavy elements (e.g., Zr) due to sediment sorting likely by bottom
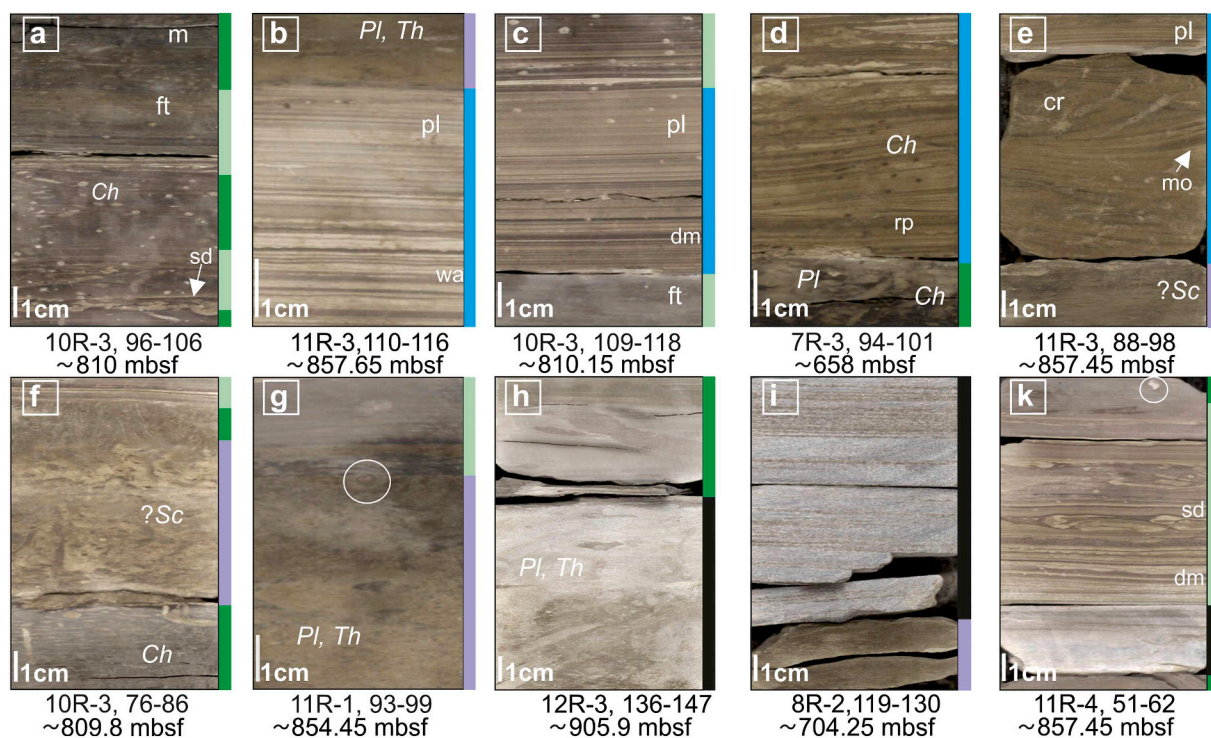
Fig. 4. Representative core photographs from facies assemblages in DSDP Hole 269A, showing main structures and bed contacts referred to in the text. Facies colour code in the sidebar to the right of each core image is according to the legend in Fig. 3. ft.: faint laminations, pl: planar laminations, wa: wavy laminations, *dm:* double mud layers, rp: ripple, cr: cross-laminations, mo: mud-offshoots, sd: soft-sedimentary structures, m: mottled, *Ch: Chondrites, Pl: Planolites, Th: Thalassinoides, Scolicia: Sc.* Note single granule in core photos: g and k. Numbers below core photos show core section and depth (mbsf).

currents.

Down-core variations of Zr/Ti ratios show high short-term variability (Fig. 3f). In general Zr/Ti show similar patterns with PC1 (Fig. S5) supporting further that both proxies reflect the accumulation of heavy minerals, due to the sorting of bottom currents and/or gravity flows. Zr/Ti ratios show less pronounced variability in fine-grained sediments between 910.5 and 901 mbsf. In general, above 858 mbsf (~24 Ma), Zr/Ti ratios show higher values (Fig. 3f). At 856.75 and 857.5 mbsf (~24 Ma) two prominent peaks of high Zr/Ti ratios, are recorded in ripple cross-laminated sandy siltstones, which indicate the strongest episodes of bottom current velocities within our study interval (Fig. S6b). In addition, high Zr/Ti ratios are shown between 752.5 and 750.17 mbsf (~23.6 Ma) (Fig. 3f).

Br/Ti ratios also increase slightly above 858 mbsf (~24 Ma). It is however between 752.5 and 655 mbsf (~23.6 Ma and 23 Ma) that ratios show increased values, which coincide with the higher preservation of microfossils in the non-carbonate cemented sediment (Fig. 3g).

The $\varepsilon_{Nd(t)}$ data from fish debris range from -9.03 ± 0.25 to -8.07 ± 0.21 (average ε_{Nd} values -8.54 ± 0.22) during the late Oligocene (~24 to 23.23 Ma) (Fig. 3h).

Late Oligocene detrital sediment samples from Site 269 have $\varepsilon_{Nd(t)}$ values of -12.14 ± 0.33 and $\varepsilon_{Nd(t)} = -13.33 \pm 0.33$, at 854.72 mbsf (~24 Ma) and 751.34 mbsf (~23.6 Ma), respectively, and are within the range of local bedrock composition of proximal areas east of the Metz glacier, within the Wilkes Subglacial Basin (Early Paleozoic granite outcrops; $\varepsilon_{Nd} = -11.2$ and -19.8; Cook et al., 2013, 2017; Bertram et al., 2018).

5.3. TEX_86

Of the 15 samples processed, 4 were flagged as outliers with potential for a biased source and thus they were not suitable for TEX_86 analysis. The remaining 11 samples had normal values in the indices

signaling overprints as mentioned in the methods. SST values were calibrated between 9 and 14 °C, $\pm$ 5.2 °C, with bioturbated facies characterized by higher SST values, compared to the laminated facies (Fig. 3i). The relative temperature variability of 3–5 °C between laminated and bioturbated sediments, respectively at Hole 269A, is consistent with sedimentological features, glacial-interglacial variability and TEX_86-derived SST reported from Site U1356 (Hartman et al., 2018; Salabarnada et al., 2018).

5.4. Palynology

All examined samples yielded well to moderately preserved palynomorphs assemblages with *Leiosphaera* (70–80%), in-situ dinocyst (20%) and pollen, while spores and reworked dinocyst are a minor component (Table S2). As is common in high polar latitudes, the absolute abundances of dinocysts remain low throughout the examined succession, and do not exceed 400 cysts/g sediment. Assemblages are dominated by P-cysts, with *Brigantedinium* spp. as most abundant (45–90% of the in situ dinocyst sum), *Lejeunecysta* (<10%) showing no clear trend throughout the section and *Selenopemphix* with its largest abundance at between 955 and 909 mbsf (30%) (Fig. 3k). Even if less abundant (rarely >5%), the samples yielded a G-cyst assemblage that mainly consists of *Batiacasphaera, Pyxidinopsis, Operculodinium* and *Impagidinium*. Similar G-cyst assemblages are present throughout the Oligocene-Miocene record from the U1356 (Bijl et al., 2018b). G-cyst are notably common between 954.3 and 950.3 mbsf (~24.2 Ma) and around 23.6 Ma, with additions of *Spiniferites spp.* (sample 9R 3 W 125–129 cm) and *G. inflata* (sample 9R 2 W 26–30 cm). Bioturbated facies contain more G-cyst compared to the laminated facies (Fig. 3k).
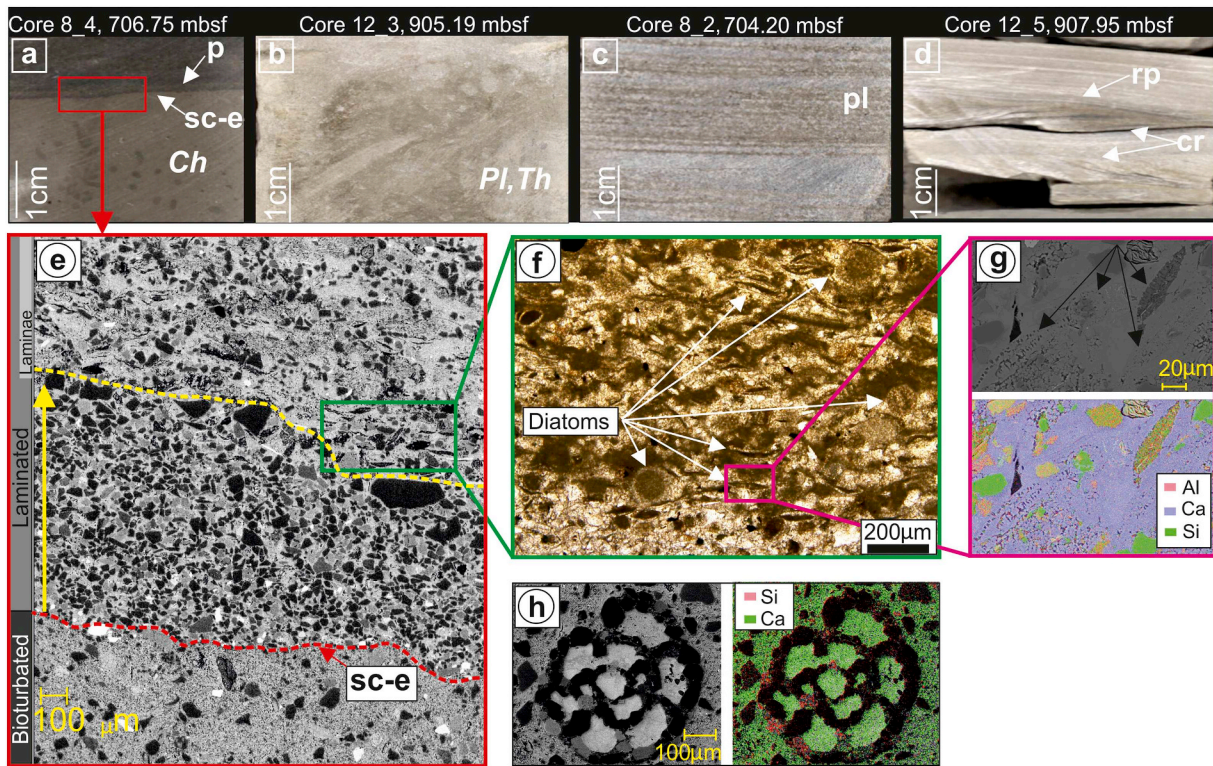
Fig. 5. Detailed images of carbonate-cemented facies. **a:** A sharp erosive contact (sc-e) between bioturbated (F3a) and laminated (F3b) carbonate-cemented facies. **b, c, d:** A carbonate-cemented bioturbated and laminated facies. **e:** Back-scattered electron photomicrograph showing blow-up example of a sharp erosive contact (sc-e) between bioturbated and laminated carbonate-cemented facies (red dotted line) and inverse grading pattern (yellow arrow) above the contact. **f:** Thin section photomicrograph, plain-polarized light of carbonate-cemented facies showing diatom assemblages within the laminae of facies F3a. **g:** HR-SEM micrograph and corresponding elemental map of Al, Ca, Si showing diatom skeletal remains within the carbonate cementation matrix. **h:** foraminifera with siliceous tests. *Ch: Chondrites, Pl: Planolites, Th: Thalassinoides,* pl: planar laminations, rp: ripple, cr: cross-laminations. (For interpretation of the references to colour in this figure legend, the reader is referred to the web version of this article.)

6. Discussion

6.1. Glacial-interglacial sedimentation and short-term polar frontal system dynamics

Repeated alternations between laminated and bioturbated facies like those described at Hole 269A (Figs. 3c and 4), are common in deep-water settings around Antarctica and are interpreted to result from changes in sedimentation related to glacial-interglacial cycles, respectively (e.g., Hepp et al., 2006; Lucchi and Rebesco, 2007; Escutia et al., 2009, 2011; Patterson et al., 2014; Salabarnada et al., 2018).

Terrigenous laminated deposits at Hole 269A (F1b, F2b, Figs. 3c and 4) are interpreted to form by a complex interplay between sediments delivered by gravity flows (e.g., debris flows and turbidity currents) and

bottom currents, during glacial times. Even when laminated deposits preserve turbidite affinity (e.g., sharp/erosional bases, normal grading depicted by visual observations and Zr/Ti variability) (e.g., Figs. S6a and S6c), we find evidence suggesting that these intervals were continuously reworked by bottom currents. This evidence include internal structures such as mud drapes, double mud layers, lenticular laminations, mud-offshoots and a rhythmic character between the intercalation of the muddy/sandy couplets with varying thicknesses (e.g., Figs. 4b, e and k). These structures are typical in contourite deposits and are interpreted to indicate both traction and suspension processes during deposition (Shanmugam et al., 1993; Rebesco et al., 2014). Additionally, the absence or scarcity and low diversity of trace fossils such as *Chondrites* and *Phycosiphon* in the laminated facies can suggest a poorly oxygenated/ventilated environment at seafloor, changes in
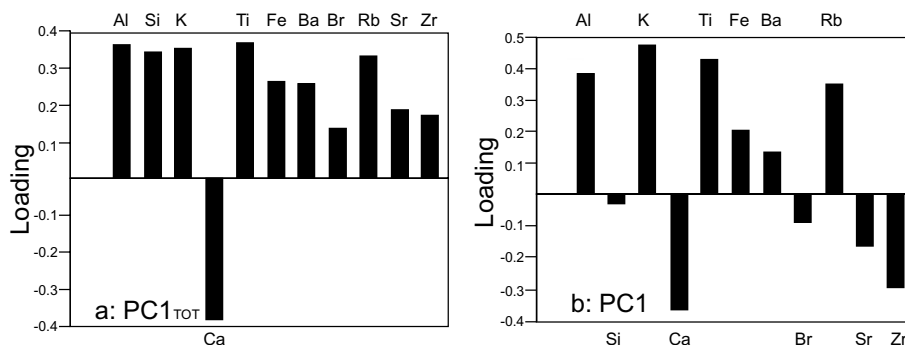

Fig. 6. Principal Component Analysis (PCA) between XRF-scanner data through the study core section. **a:** $PC1_{TOT}$ with carbonate-cemented facies and **b:** PC1 without carbonate-cemented facies.

nutrient availability and likely high sedimentation rates that promote unfavorable conditions for trace markers to thrive (e.g., Lucchi and Rebesco, 2007; Rodriguez-Tovar and Dorador, 2014; Rodríguez-Tovar et al., 2014; Rodríguez-Tovar and Dorador, 2015; Rodríguez-Tovar et al., 2015b; Hodell et al., 2017; Rodríguez-Tovar et al., 2019). Poorly ventilated conditions at the seafloor were also reported from late Oligocene laminated facies at Site U1356, during glacial times (Salabarnada et al., 2018).

In comparison, bioturbated facies (F1a, F2a, Figs. 3c and 4) are interpreted to result from mainly hemipelagic sedimentation during interglacial times with continued reworking by bottom currents. The inverse and bi-gradational grading patterns shown by Zr/Ti ratios and MS variations, when resolution is sufficient (Fig. S6) is a strong evidence of bottom current control, suggesting winnowing by bottom currents with fluctuating intensities (e.g., Stow and Faugères, 2008). The diverse trace fossil assemblage, indicate more oxygenated/better ventilated conditions, likely higher nutrient content in the seafloor and lower sedimentation favorable to microbenthic trace marker proliferation than during glacial times (e.g., Lucchi and Rebesco, 2007; Rodríguez-Tovar et al., 2015a, 2015b). Late Oligocene bioturbated deposits from Site U1356 also record an increase in oxygenation at the seafloor when compared with laminated deposits of the same age at the site (Salabarnada et al., 2018).

The carbonate-cemented laminated and bioturbated facies (facies: F3a, F3b; Figs. 3c and 5) are interpreted to result from sedimentation during the warmest interglacials recorded by our sediments. This is indicated by the high Ca content (Fig. 3d) associated with dissolution of calcareous microfossils, which strongly supports the biogenic origin of these carbonate beds (Fig. 5f, g and h).

Our interpretation of sediments recovered at Site 269 from 956 to 858 mbsf (before 24 Ma) is supported by similar late Oligocene (26–25 Ma) bioturbated and laminated sediments recovered at the more proximal IODP Site U1356. Nearly continuous recovery of this interval at Site U1356, allowed for a detailed study of glacial-interglacial cyclicity that is paced by obliquity (Salabarnada et al., 2018). These authors interpreted the changes between laminated and bioturbated facies at Site U1356 to be driven by oceanic frontal migrations forced by glacial-interglacial cycles. In detail, during interglacial times, southward migration of the SWW and the surface oceanic fronts facilitated proto-CDW intrusions closer to the Antarctic margin. This allowed better preservation of calcareous microfossils and enhanced ventilation at the seafloor. The opposite occurred during the glacial times. In addition, even when the interval from 26 and 25 Ma was generally warm as indicated by the prevalence of open water conditions (Bijl et al., 2018a, 2018b), TEX$_{86}$-derived SST variations (between 1.5 and 3 °C) (Hartman et al., 2018) correlate with the glacial-interglacial cyclicity reported by Salabarnada et al. (2018). In fact, our more distal TEX$_{86}$-based SST data and dinocyst assemblages, compared to those from Site U1356 (Hartman et al., 2018; Bijl et al., 2018b) support further the oceanic frontal migrations forced by glacial-interglacial cycles. The relative SST variability of 3–5 °C at Site 269 may be slightly higher than the glacial-interglacial TEX$_{86}$-derived SST variability from Site U1356 during the Oligocene-Miocene (Hartman et al., 2018), although a full representation of the glacial-interglacial variability at either site might not have been captured. Additionally, the high abundance of *Brigantedinium spp* (P-cyst) reflect open ocean upwelling and high-nutrient conditions (Harland and Pudsey, 1999; Zonneveld et al., 2013) at Site 269, perhaps even more than at U1356. In addition, the lower amounts of G-cysts compared to Site U1356 indicate that Site 269 was located closer to the upwelling/divergence zone during the glacial times. In contrast, SST increase and higher amounts of G-cysts (lower P/G cyst ratios) similar to modern temperate (interglacial), oligotrophic waters from around Tasmania and southern New Zealand (Prebble et al., 2013) indicate the southward migration of the oceanic fronts during the interglacial times. Our results are consistent with dinocyst assemblages at Site U1356, which show similar changes between

oligotrophic, temperate dinocyst assemblages during interglacials, to eutrophic, colder dinocysts during glacial times (Bijl et al., 2018b). The difference in dinocyst assemblages between the two sites may be attributed to a closer proximity of Site 269 to the Antarctic Divergence.

Deposition of large stacked debris flow deposits at Site U1356 between ~24.76 Ma and 23.23 Ma (Escutia et al., 2011; Passchier et al., 2018) provide limited information regarding ocean configurations during the late Oligocene-early Miocene in this region of the East Antarctic margin. This gap is recorded at Site 269 despite the limitations related to the discontinuous drilling and low-resolution age model. Our sedimentological, geochemical and palynological analyses show that the climate-related ocean polar frontal movement migrations continued throughout the late Oligocene and into the early Miocene. We also note an increase in the frequency of siltstones and sandstones beds between 24 and 23.23 Ma. These sediments could result from local inputs from structural highs depicted nearby in seismic lines that cross the site (De Santis et al., 2003). We note however that Oligocene and the Miocene deposition around these highs is dominated by contourite deposition forming mounded deposits against the highs (De Santis et al., 2003), which could prevent direct delivery of sediment to where Site 269 is located. The correlations previously established between sedimentation at Sites 269 and U1356, argues for a regional source of sediments to Site 269 rather than a local one. We therefore argue that these coarse sediments likely correspond to the distal reaches of the debris flow deposits recovered at Site U1356. At this site these deposits have been interpreted to result from ice sheet advances into the continental shelf (Escutia et al., 2011, 2014).

6.2. Bottom water signatures at Site 269

Geological evidence derived from microfossil assemblages from sedimentary records around Antarctica, including evidence from Site 269, suggest that the proto-Polar Front (PF) was placed close to 60°S between the late Oligocene-early Miocene (Nelson and Cooke, 2001; Cooke et al., 2002). This is further supported by dinocyst assemblage data from Hole 269A indicating that the site was influenced by nutrient-rich upwelling and ice-free waters, with occasionally southward latitudinal transport of waters during the late Oligocene and early Miocene. Fish debris neodymium isotope results from Site 269 (Fig. 3h) are consistent with late Oligocene proto-CDW $\varepsilon_{Nd(t)}$ values recorded along the proto-PF on the Kerguelen Plateau (Indian Ocean) (average $\varepsilon_{Nd(t)} = -7.8$; Wright et al., 2018) and around Maud Rise (Atlantic Ocean) (average $\varepsilon_{Nd(t)} = -8.5$; Scher and Martin, 2004). The combined dataset suggests that a common bottom water mass (proto-CDW) was bathing the South Atlantic and South Indian Ocean along the proto-PF. The pronounced difference between the $\varepsilon_{Nd(t)}$ values of the fish debris and the detrital sediment samples from Site 269 ($\varepsilon_{Nd(t)} = -12.14 \pm 0.33$, -13.33 ± 0.33 (~24 Ma and ~23.6 Ma, respectively) confirm the water mass signal in the fish debris samples (Fig. S7). Bathymetric reconstructions show that the Southern Indian Ocean basin was already sufficiently deep during the Oligocene and did not contain any large topographic barriers that prevented the flow of proto-CDW from the Kerguelen Plateau to the abyssal plain off the Australian-Antarctic basin (Scotese and Wright, 2018). Based on the above, we conclude that at least during the latest Oligocene (~24 to ~23.23 Ma), Site 269 was covered by a proto-CDW with a Nd signature similar to the present day CDW in the Australian sector of Southern Ocean ($\varepsilon_{Nd} = -8.1$ to -9.1; Lambelet et al., 2018). This observation contrasts with the present-day bottom water mass configuration at the location of Site 269, which is bathed by Adélie Land Bottom Water (ALBW) (Rintoul, 1998), suggesting a reduced export of ALBW during the late Oligocene. These results are consistent with previous inferences for reduced sea ice in the region (Bijl et al., 2018b; Hartman et al., 2018) diminishing production of ALBW at the Oligocene and Miocene on the Wilkes Land shelf. The less radiogenic $\varepsilon_{Nd(t)}$ value around 24 Ma ($\varepsilon_{Nd(t)} = -9.03 \pm 0.25$) may suggest mixing between proto-CDW and Adélie Coast Bottom Water

(ACBW; Oligocene ACBW $\varepsilon_{Nd(t)} = -10.6 \pm 0.8$; Huck et al., 2017). However, more data are needed to confirm this hypothesis.

6.3. Long-term changes in the proto-ACC dynamics during the late Oligocene to earliest Miocene

We provide new insights into the ocean configuration during four distinct periods between the late Oligocene-early Miocene from ~24.2 to 24 Ma, at ~24 Ma, from ~23.6 to 23.23 Ma, and at ~23 Ma.

A remarkable shift in sedimentation occurs at ~24 Ma (858 mbsf) (Fig. 3a). Before 24 Ma, predominantly fine-grained sediment deposited under enhanced terrigenous inputs and an overall weak proto-CDW. This interpretation is supported by the high Ti values and low Zr/Ti ratios, respectively, and their low variability, in particular between 910 and 901 mbsf (Fig. 3e and f). Furthermore, less frequent bioturbated facies and low Br/Ti ratios suggest a less ventilated environment and low nutrient content at the seafloor (Fig. 3b and g). The high abundance of G-cyst assemblages between 954.3 and 950.3 mbsf (Fig. 3k), together with high SST (11.5 to 14 °C) (Fig. 3i), indicate that the polar front system was located south of the Site 269. However, the concomitant SST drop to 9 °C and the absence of G-cysts at 948 mbsf (Fig. 3i and k) indicate northward migration of the polar front, which likely reached Site 269.

Around 24 Ma, our data document the strongest proto-CDW velocities recorded at Hole 269A during the late Oligocene and earliest Miocene, as indicated by the high Zr/Ti peaks associated with cross-sandy laminated intervals that are not preserved elsewhere in the sedimentary record (Figs. 3f and 4e).

After 24 Ma, there is an increase in the frequency of deposition of coarser-grained material interbedded with fine-grained sediment (Fig. 3a). Overall Zr/Ti ratios are higher suggesting periods of proto-CDW strengthening, with Zr/Ti peaks associated with Ca enrichment (Figs. 3f and 6b). In addition, more abundant and diverse bioturbation (Fig. 3b and c) point to episodes of better ventilated bottom conditions, and likely higher nutrient content at the seafloor, as indicated by a small increase in Br/Ti ratios (Fig. 3g). Between ~24 and 23.6 Ma, the frontal system migrated northward, as indicated by the lower SST (9.8–10.8 °C) and the dominance of P-cysts, suggesting cool and eutrophic ocean conditions. In addition, the sheer absence of dinocysts may have resulted from low preservation associated to oxidation at sea floor, transport by bottom currents and/or reduced productivity. Given the warmth as reconstructed for the surrounding time intervals (e.g., Bijl et al., 2018b; Hartman et al., 2018), we rule out a permanent ice cover during this time.

We infer that the observed shift in depositional environment at 24 Ma was driven by atmospheric and oceanic frontal changes. SWW northward migration due to the major expansion of the AIS between 24.5 and 24 Ma (see Levy et al., 2019 for discussion) is thought to have forced the northward migration of the SWW prior to 24 Ma (Fig. 7a and c). This would have resulted in a weak proto-CDW, reduced water mass mixing, and a less ventilated seafloor. In contrast, the increase in proto-CDW intensification after 24 Ma, inferred from the higher Zr/Ti amplitudes, likely indicate times when SWW migrated southwards, aligned with the proto-ACC. This promoted enhanced mixing and better ventilation of the seafloor and likely higher organic matter deposition, in times when the AIS retreated. Our SST and dinocyst data further support the warmer temperatures and dominance of G-cysts, which indicate the stronger influence of warm oligotrophic waters.

Between ~23.6 and ~23.23 Ma, sediments record a prominent southward polar frontal system migration, which allowed warmer water to penetrate further southwards (Fig. 7a and c). This interval is characterized by high Zr/Ti ratios (at ~23.6 Ma, Fig. 3f), high Ca, high SST (11.5–12.9 °C) (Fig. 3i) and a reduction in terrigenous input (low Ti values) (Fig. 3d and e). In addition, there is higher preservation of calcareous microfossils in some intervals (Fig. S4), and dominance of G-cysts (Fig. 3k), similar to those in modern temperate (interglacial),

oligotrophic waters from around Tasmania and southern New Zealand (Prebble et al., 2013), high Br/Ti ratios (Fig. 3g) and a thick carbonate cemented bed at ~23.23 Ma (Fig. 3a). Today, calcareous organisms rarely reach the seafloor within and south of the polar front zone. This is because of the presence of the corrosive (CO_2-rich) Antarctic deep waters (Whitehead and Bohaty, 2003 and references therein) and strong upwelling (Olbers et al., 2004), which dissolve calcareous rain. A thick carbonate cemented bed is present at Site U1356 dated at 23.23 Ma (Escutia et al., 2011). The synchronous deposition of these carbonate-cemented beds at Sites U1356 and 269 strongly supports a wide southward expansion of proto-CDW offshore Wilkes Land at ~23.23 Ma. Our ε_{Nd} data, despite their low resolution, also suggest a greater influence of proto-CDW during this period compared to ~24 Ma (Fig. 3h). Similar processes occur today, when a reduction in the volume of AABW is compensated by the expansion of CDW (van Wijk and Rintoul, 2014). Our interpretation is further supported by the absence of sea-ice-related dinocyst species (i.e. *Selenopemphix antarctica*) at both Sites 269 and U1356 (Bijl et al., 2018b), which suggests a weaker than modern sea ice season during the Oligocene and Miocene. In addition, the new SST reconstruction at Site 269, similar to those at Site U1356, report warmer surface water conditions than today and argue for a decrease in the potential formation of Antarctic bottom waters (Hartman et al., 2018).

At ~23 Ma, high Br/Ti ratios indicate an increase in the organic content in the sediment (Fig. 3), coinciding with the first evidence (scarce) of diatoms at Site 269. A shift from calcareous dominated microfossils to siliceous (e.g., diatomaceous and cherty clay sediments) has also been reported at Site U1356 (Escutia et al., 2011, 2014; Passchier et al., 2018) arguing for a major regional event likely related to the AIS expansion during the early Miocene, northward expansion of the polar front system and more influence of siliceous productivity. This is supported by the high amount of P-cyst at Site 269 at ~23 Ma, which indicate cool, nutrient-rich upwelling conditions (Fig. 3k). After 23 Ma, deposition of the thickest carbonate cemented bed would imply this period was followed by a southward migration of the frontal system (Fig. 3a).

In summary, our combined sedimentological, geochemical and palynological data between ~24.2 and ~23 Ma show a dynamic proto-ACC off the Wilkes Land margin during the late Oligocene-Miocene. In addition, the carbonate preservation and low siliceous microfossil preservation at Site 269 (located within the polar front zone) contrasts with modern sedimentation near the Polar Front. This is supported by the presence of oligotrophic, temperate dinocyst assemblages at Sites 269 and U1356 that are similar to the ones found today north of the Polar Front around Tasmania and the Southern New Zealand (Bijl et al., 2018b). Our data therefore suggest a weaker frontal system, characterized by reduced upwelling, which probably allowed southward transport of warm surface waters from lower latitude. This is consistent with numerical modeling results indicating a weaker than present-day proto-ACC (Herold et al., 2012; Hill et al., 2013). These findings argue against the onset of a modern-like ACC during the latest Oligocene (ca 25–23 Ma) based on sedimentary records across the Tasman Gateway (Pfuhl and McCave, 2005) and the South Pacific (Lyle et al., 2007).

7. Conclusions

Our integrated sedimentological, geochemical, isotopic and palynological data sets from DSDP Site 269 provide new insights into the proto-ACC dynamics during the late Oligocene-early Miocene (~24.2 to 23 Ma) off the eastern Wilkes Land margin. We show that sedimentation at Site 269 is controlled by the persistent reworking of gravity flows and hemipelagic sedimentation by proto-CDW that is characterized by fluctuating current intensities driven by the migration of the frontal system in response to climatic changes. We detail four distinct snapshots (from ~24.2 to 24 Ma, at ~24 Ma, from ~23.6 to ~23.23 Ma, and at ~23 Ma) that we link to changes in the proto-ACC

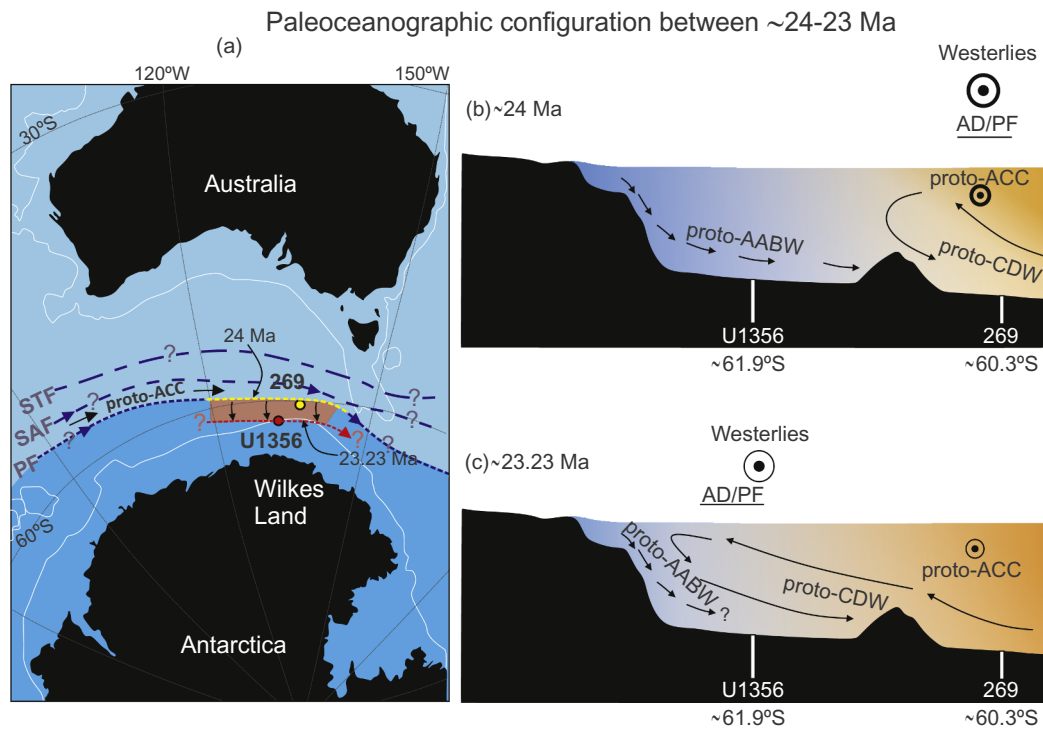## Paleoceanographic configuration between ~24-23 Ma

Fig. 7. Paleoceanographic configuration offshore the Wilkes Land margin around 24–23 Ma. **a:** Reconstructed ocean frontal system between Antarctica and Australia around 24–23 Ma. Reconstruction of tectonic plates around Tasman Gateway and paleoposition of sites based on Seton et al., 2012 global plate motion model derived from Gplates software (Müller et al., 2018). White lines indicate the continental lithosphere boundary. Polar water south of the PF are shaded in darker blue. Boundary between polar and subantarctic waters during the 23.23 Ma (red dashed line) and during the 24 Ma (yellow dashed line). Frontal constraints west and east of the Wilkes Land region are from reconstructions of Nelson and Cooke (2001); Cooke et al. (2002). STF: Subtropical front, SAF Subantarctic front, PF: Polar front. Black arrows show the pathway of the proto-ACC. Schematic illustrations of proto-CDW dynamics for the 24 Ma (b) and 23.23 Ma (c). **b:** At ~24 Ma, Westerlies and PF were located close to Site 269 resulting strong proto-ACC. There is likely enhanced proto-AABW production. **c:** At ~23.23 Ma, Westerlies and PF migrated southwards close to Site U1356. Proto-ABBW formation is reduced. This allowed the relative warmer surface water and proto-CDW to penetrate closer to Antarctic continent. (For interpretation of the references to colour in this figure legend, the reader is referred to the web version of this article.)

and deep proto-CDW dynamics. Just before 24 Ma, fine-grained sediments were deposited under enhanced terrigenous inputs and weak proto-CDW intensities that resulted in low ventilated bottom conditions and probably low organic content and preservation. At 24 Ma, episodic events of stronger proto-CDW current velocities started, associated with coarser-grained deposits, and better ventilated bottom conditions and slightly higher organic matter content. In addition, TEX_{86}-derived SST data varied between 9 and 13.5 °C, while the dominance of P -cysts indicate relatively cool ocean temperatures, upwelling and high-nutrient conditions between ~24 and 23.6 Ma. Together, these evidences suggest that the polar front at this time was located near the site. At ~23.6 Ma, and more pronounced at ~23.23 Ma, a prolonged expansion of proto-CDW closer to the Wilkes Land margin is indicated by the higher Ca values, better preservation of calcareous microfossils, higher Br/Ti ratios, high SST (from 11.5 to 12.9 °C), high amounts of G-cysts similar to modern temperate and oligotrophic waters, and ε_{Nd} data resembling modern-like CDW ε_{Nd} signature at Site 269. Given that the record between ~24.9 and 23.23 Ma was masked by debris flow deposition at the more proximal IODP Site U1356, our results provide the first record of ocean configuration for this margin for this time interval. When compared with results from Site U1356 and with numerical modeling, our findings support the notion of a fundamentally different Southern Ocean with a weaker proto-ACC than today during the late Oligocene and earliest Miocene. A weaker frontal system permitted the incursion of warm waters from lower latitude closer to the Antarctic margin and the preservation of carbonate. The synchronous deposition of thick carbonate-cemented beds both at Site 269 and U1356 at 23.23 Ma indicates a regional event of poleward proto-CDW expansion.

Declaration of Competing Interest

The authors declare that they have no known competing financial interests or personal relationships that could have appeared to influence the work reported in this paper.

Appendix A. Supplementary data

Supplementary data to this article can be found online at https://doi.org/10.1016/j.gloplacha.2020.103221.

References

Anderson, J.B., Bartek, L.R., 1992. Cenozoic glacial history of the Ross Sea revealed by intermediate resolution seismic reflection data combined with drill site information, the Antarctic Paleoenvironment: A Perspective on Global Change: Part One. pp. 231–263. https://doi.org/10.1029/AR056p0231.

Aoki, S., Bindoff, N.L., Church, J.A., 2005. Interdecadal water mass changes in the Southern Ocean between 30°E and 160°E. Geophys. Res. Lett. 32, L07607. https://doi.org/10.1029/2004GL022220.

Bahr, A., Jiménez-Espejo, F.J., Kolasinac, N., Grunert, P., Hernández-Molina, F.J., Röhl, U., Voelker, A.H.L., Escutia, C., Stow, D.A.V., Hodell, D., Alvarez-Zarikian, C.A., 2014. Deciphering bottom current velocity and paleoclimate signals from contourite deposits in the Gulf of Cádiz during the last 140 kyr: an inorganic geochemical approach. Geochem. Geophy. Geosy. 15, 3145–3160. https://doi.org/10.1002/2014GC005356.

Barrett, P.J., 1975. Textural characteristics of Cenozoic preglacial and glacial sediments at Site 270, Ross Sea, Antarctica. Initial Rep. Deep Sea Drilling Project 28, 757–766.

Beddow, H.M., Liebrand, D., Sluijs, A., Wade, B.S., Lourens, L.J., 2016. Global change across the Oligocene-Miocene transition: High-resolution stable isotope records from IODP Site U1334 (equatorial Pacific Ocean). Paleoceanography 31, 81–97. https://doi.org/10.1002/2015PA002820.

Bertram, R.A., Wilson, D.J., van de Flierdt, T., McKay, R.M., Patterson, M.O., Jimenez-Espejo, F.J., Escutia, C., Duke, G.C., Taylor-Silva, B.I., Riesselman, C.R., 2018. Pliocene deglacial event timelines and the biogeochemical response offshore Wilkes Subglacial Basin, East Antarctica. Earth Planet. Sci. Lett. 494, 109–116. https://doi.org/10.1016/j.epsl.2018.04.054.

Bijl, P.K., Bendle, J.A., Bohaty, S.M., Pross, J., Schouten, S., Tauxe, L., Stickley, C.E., McKay, R.M., Rohl, U., Olney, M., Sluijs, A., Escutia, C., Brinkhuis, H., and Expedition 318 Scientists., 2013. Eocene cooling linked to early flow across the Tasmanian Gateway. Proc. Natl. Acad. Sci., 110 (24), pp. 9645–9650.

Bijl, P.K., Houben, A.J.P., Bruls, A., Pross, J., Sangiorgi, F., 2018a. Stratigraphic calibration of Oligocene–Miocene organic-walled dinoflagellate cysts from offshore Wilkes Land, East Antarctica, and a zonation proposal. J. Micropalaeontol. 37, 105–138. https://doi.org/10.5194/jm-37-105-2018.

Bijl, P.K., Houben, A.J.P., Hartman, J.D., Pross, J., Salabarnada, A., Escutia, C., Sangiorgi, F., 2018b. Paleoceanography and ice sheet variability offshore Wilkes Land, Antarctica – part 2: Insights from Oligocene–Miocene dinoflagellate cyst assemblages, Clim. Past 14, 1015–1033. https://doi.org/10.5194/cp-14-1015-2018.

Blaga, C.I., Reichart, G.-J., Heiri, O., Damsté, J.S.S., 2009. Tetraether membrane lipid distributions in water-column particulate matter and sediments: a study of 47 European lakes along a north–south transect. J. Paleolimnol. 41 (3), 523–540.

Cook, C.P., van de Flierdt, T., Williams, T., Hemming, S.R., Iwai, M., Kobayashi, M., Jimenez-Espejo, F.J., Escutia, C., Gonzalez, J.J., Khim, B.-K., McKay, R.M., Passchier, S., Bohaty, S.M., Riesselman, C.R., Tauxe, L., Sugisaki, S., Galindo, A.L., Patterson, M.O., Sangiorgi, F., Pierce, E.L., Brinkhuis, H., Klaus, A., Fehr, A., Bendle, J.A.P., Bijl, P.K., Carr, S.A., Dunbar, R.B., Flores, J.A., Hayden, T.G., Katsuki, K., Kong, G.S., Nakai, M., Olney, M.P., Pekar, S.F., Pross, J., Rohl, U., Sakai, T., Shrivastava, P.K., Stickley, C.E., Tuo, S., Welsh, K., Yamane, M., 2013. Dynamic behaviour of the East Antarctic ice sheet during Pliocene warmth. Nat. Geosci. 6 (9), 765–769. https://doi.org/10.1038/ngeo1889.

Cook, C.P., Hemming, S.R., van de Flierdt, T., Pierce Davis, E.L., Williams, T., Galindo, A.L., Jiménez-Espejo, F.J., Escutia, C., 2017. Glacial erosion of East Antarctica in the Pliocene: a comparative study of multiple marine sediment provenance tracers. Chem. Geol. 466, 199–218.

Cooke, P.J., Nelson, C.S., Crundwell, M.P., Spiegler, D., 2002. Bolboforma as monitors of Cenozoic palaeoceanographic changes in the Southern Ocean, Palaeogeography, Palaeoclimatology. Palaeoecology 188 (1), 73–100.

Crouch, E.M., Willumsen, P.S., Kulhanek, D.K., Gibbs, S.J., 2014. A revised Paleocene (Teurian) dinoflagellate cyst zonation from eastern New Zealand. Rev. Palaeobot. Palynol. 202, 47–79.

Dale, B., 1996. Dinoflagellate cyst ecology: modeling and geological applications. Palynology: principles and applications 1249–1275.

Damsté, J.S.S., Ossebaar, J., Abbas, B., Schouten, S., Verschuren, D., 2009. Fluxes and distribution of tetraether lipids in an equatorial African lake: constraints on the application of the TEX86 palaeothermometer and BIT index in lacustrine settings. Geochim. Cosmochim. Acta 73 (14), 4232–4249.

De Santis, L., Brancolini, G., Donda, F., 2003. Seismo-stratigraphic analysis of the Wilkes Land continental margin (East Antarctica): influence of glacially driven processes on the Cenozoic deposition. Deep-Sea Res. II Top. Stud. Oceanogr. 50 (8–9), 1563–1594. https://doi.org/10.1016/S0967-0645(03)00079-1.

DePaolo, Wasserburg, G.L., 1976. Nd isotopic variations and petrogenetic models. Geophys. Res. Lett. 3, 249–252.

Dorador, J., Rodríguez-Tovar, F.J., 2014. A novel application of digital image treatment by quantitative pixel analysis to trace fossil research in marine cores. PALAIOS 29 (10), 533–538.

Dorador, J., Rodríguez-Tovar, F.J., IODP Expedition 339 Scientists, 2014a. Digital image treatment applied to ichnological analysis of marine core sediments. Facies 60 (1), 39–44.

Dorador, J., Rodríguez-Tovar, F.J., IODP Expedition 339 Scientists, 2014b. Quantitative

estimation of bioturbation based on digital image analysis. Mar. Geol. 349, 55–60.

Dorador, J., Rodríguez-Tovar, F.J., 2018. High-resolution image treatment in ichnological core analysis: initial steps, advances and prospects. Earth-Sci. Rev. 177, 226–237.

Escutia, C., Bárcena, M.A., Lucchi, R.G., Romero, O., Ballegeer, A.M., Gonzalez, J.J., Harwood, D.M., 2009. Circum-Antarctic warming events between 4 and 3.5 Ma recorded in marine sediments from the Prydz Bay (ODP Leg 188) and the Antarctic Peninsula (ODP Leg 178) margins, Glob. Planet. Change 69, 170–184. https://doi.org/10.1016/j.gloplacha.2009.09.003.

Escutia, C., Brinkhuis, H., Klaus, A., the Expedition 318 Scientists, 2011. Wilkes Land Glacial History: Cenozoic East Antarctic Ice Sheet evolution from Wilkes Land margin sediments. Proceedings of the Integrated Ocean Drilling Program, Volume 318. In: Integrated Ocean Drilling Program Management International Inc.

Escutia, C., Brinkhuis, H., the Expedition 318 Science Party, 2014. From Greenhouse to Icehouse at the Wilkes Land Antarctic margin: IODP 318 synthesis of results. In: Stein, R., Blackman, D.K., Inagaki, F., Larsen, H.-C. (Eds.), Earth and Life Processes Discovered fromSubseafloor Environment. Vol. 7. Elsevier, Amsterdam, pp. 295–328.

Escutia, C., DeConto, R.M., Dunbar, R., De Santis, L., Shevenell, A., Naish, T., T., 2019. Keeping an eye on Antarctic Ice Sheet stability. Oceanography 32 (1), 32–46. https://doi.org/10.5670/oceanog.2019.117.

Esper, O., Zonneveld, K.A.F., 2002. Distribution of organic-walled dinoflagellate cysts in surface sediments of the Southern Ocean (eastern Atlantic sector) between the Subtropical Front and the Weddell Gyre. Mar. Micropaleotol. 46, 177–208.

Ferrari, R., Jansen, M.F., Adkins, J.F., Burke, A., Stewart, A.L., Thompson, A.F., 2014. Antarctic Sea ice control on ocean circulation in present and glacial climates. Proc. Natl. Acad. Sci. U. S. A. 111 (24), 8753–8758. https://doi.org/10.1073/pnas.1323922111.

Foster, G.L., Rohling, E.J., 2013. Relationship between sea level and climate forcing by CO2 on geological timescales. P. Natl. Acad. Sci. USA 110, 1209–1214. https://doi.org/10.1073/pnas.1216073110.

Frank, M., 2002. Radiogenic isotopes: Tracers of past ocean circulation and erosional input: Reviews of Geophysics. v. 40https://doi.org/10.1029/2000RG000094.

Goldstein, S.L., Hemming, S.R., 2003. 6.17 - Long-lived isotopic tracers in oceanography, paleoceanography, and ice-sheet dynamics. In: Holland, H.D., Turekian, K.K. (Eds.), Treatise on Geochemistry. Pergamon, Oxford, pp. 453–489.

Gradstein, F.M., Ogg, J.G., Schmitz, M.D., Ogg, G.M., 2012. The Geologic Time Scale 2012. 2. pp. 437–1144.

Grützner, J., Hillenbrand, C.-D., Rebesco, M., 2005. Terrigenous flux and biogenic silica deposition at the Antarctic continental rise during the late Miocene to early Pliocene: implications for ice sheet stability and sea ice coverage. Glob. Planet. Chang. 45, 131–149.

Hammer, Ø., Harper, D.A.T., Ryan, P.D., 2001. PAST: Paleontological statistics software package for education and data analysis. Palaeontol. Electron. 4 (1), 9.

Harland, R., Pudsey, C.J., 1999. Dinoflagellate cysts from sediment traps deployed in the Bellingshausen, Weddell and Scotia seas, Antarctica. Mar. Micropaleotol. 37, 77–99.

Hartman, J.D., Sangiorgi, F., Salabarnada, A., Peterse, F., Houben, A.J.P., Schouten, S., Escutia, C., Bijl, P.K., 2018. Paleoceanography and Ice Sheet Variability Offshore Wilkes Land, Antarctica – Part 3 : Insights from Oligocene – Miocene TEX 86 -Based Sea Surface Temperature Reconstructions. pp. 1275–1297.

Hayes, D.E., Frakes, L.A., et al., 1975. Initial Reports of the Deep Sea Drilling Project' vol. 28. U.S. Government Printing Office, Washington, pp. 179–210. https://doi.org/10.2973/dsdp.proc.28.107.1975.

Head, M., 1996. Modern dinoflagellate cysts and their biological affinities. Palynology: principles and applications 3, 1197–1248.

Hepp, D.A., Mörz, T., Grützner, J., 2006. Pliocene glacial cyclicity in a deep-sea sediment drift (Antarctic Peninsula Pacific margin). Palaeogeogr. Palaeoclimatol. Palaeoecol. 231, 181–198.

Hernández-Sánchez, M.T., Woodward, E.M.S., Taylor, K.W.R., Henderson, G.M., Pancost, R.D., 2014. Variations in GDGT distributions through the water column in the South East Atlantic Ocean. Geochim. Cosmochim. Acta 132, 337–348. https://doi.org/10.1016/j.gca.2014.02.009.

Herold, N., Huber, M., Müller, R.D., Seton, M., 2012. Modeling the Miocene Climatic Optimum : Ocean Circulation. 27. pp. 1–22. https://doi.org/10.1029/2010PA002041. (December 2011).

Hill, D.J., Haywood, A.M., Valdes, P.J., Francis, J.E., Lunt, D.J., Wade, B.S., Bowman, V.C., 2013. Paleogeographic controls on the onset of the Antarctic circumpolar current. Geophys. Res. Lett. 40, 5199–5204. https://doi.org/10.1002/grl.50941.

Ho, S.L., Laepple, T., 2015. Glacial cooling as inferred from marine temperature proxies TEX_{86}^H and $U_{37}^{K'}$. Earth Planet. Sci. Lett. 409, 15–22. https://doi.org/10.1016/j.epsl.2014.10.033.

Ho, S.L., Mollenhauer, G., Fietz, S., Martínez-Garcia, A., Lamy, F., Rueda, G., Schipper, K., Méheust, M., Rosell-Melé, Stein, R., Tiedemann, R. Stein, R., 2014. Appraisal of TEX86 and TEX86L thermometries in subpolar and polar regions. Geochim. Cosmochim. Acta, 131, 213–226.

Hodell, D.A., Nicholl, J.A., Bontognali, T.R.R., Danino, S., Dorador, J., Dowdeswell, J.A., Einsele, J., Kuhlmann, H., Martrat, B., Mleneck-Vautravers, M.J., Rodriguez-Tovar, F.J., Rohl, U., 2017. Anatomy of Heinrich Layer 1 and its role in the last deglaciation. Paleoceanography 32, 284–303.

Hopmans, E.C., Weijers, J.W., Schefuß, E., Herfort, L., Damsté, J.S.S., Schouten, S., 2004. A novel proxy for terrestrial organic matter in sediments based on branched and isoprenoid tetraether lipids. Earth Planet. Sci. Lett. 224 (1–2), 107–116.

Hopmans, E.C., Schouten, S., Sinninghe Damsté, J.S., 2015. The effect of improved chromatography on GDGT-based palaeoproxies. Org. Geochem. https://doi.org/10.1016/j.orggeochem.2015.12.006.

Huck, C.E., van de Flierdt, T., Bohaty, S.M., Hammond, S.J., 2017. Antarctic climate, Southern Ocean circulation patterns, and deep water formation during the Eocene.

Paleoceanography 32, 674–691. https://doi.org/10.1002/2017PA003135.

IPCC, 2013. Climate Change 2013: The Physical Science Basis, Contribution of Working Group I to the Fifth Assessment Report of the Intergovernmental Panel on Climate Change. Cambridge University Press, Cambridge, United Kingdom and New York, NY, USA.

Jacobsen, S.B., Wasserburg, G., 1980. Sm-Nd isotopic evolution of chondrites. Earth Planet. Sci. Lett. 50 (1), 139–155.

Jimenez-Espejo, F.J., Martinez-Ruiz, F., Sakamoto, T., Iijima, K., Gallego-Torres, D., Harada, N., 2007. Paleoenvironmental changes in the western Mediterranean since the last glacial maximum: High resolution multiproxy record from the Algero-Balearic basin. Palaeogeogr. Palaeoclimatol. Palaeoecol. 246, 292–306. https://doi.org/10.1016/j.palaeo.2006.10.005.

Jovane, L., Florindo, F., Acton, G., Ohneiser, C., Sagnotti, L., Strada, E., Verosub, K.L., Wilson, G.S., Iacoviello, F., Levy, R.H., Passchier, S., 2019. Miocene glacial dynamics recorded by variations in magnetic properties in the ADRILL-2A drill core. Am. Geophys. Union. https://doi.org/10.1029/2018JB016865.

Kim, J.H., Van der Meer, J., Schouten, S., Helmke, P., Willmott, V., Sangiorgi, F., Koç, H., Hopmans, E.C., Sinninghe Damsté, J.S., 2010. New indices and calibrations derived from the distribution of crenarchaeal isoprenoid tetraether lipids: Implications for past sea surface temperature reconstructions. Geochim. Cosmochim. Acta 74 (16), 4639–4654.

Kulhanek, D., Levy, R., Clowes, C.D., Prebble, J.G., Rodelli, D., Jovane, L., Morgans, H.E.G., Kraus, C., Zwingmann, H., Griffith, E.M., Scher, H.D., McKay, R.M., Naish, T.R., 2019. Revised chronostratigraphy of DSDP Site 270 and late Oligocene to early Miocene paleoecology of the Ross Sea sector of Antarctica. Glob. Planet. Chang. 178, 46–64.

Lambelet, M., van de Flierdt, T., Butler, E.C.V., Bowie, A.R., Rintoul, S.R., Watson, R.J., Remenyi, T., Lannuzel, D., Warner, M., Robinson, L.F., Bostock, H.C., Bradtmiller, L.I., 2018. The neodymium isotope fingerprint of Adélie Coast Bottom Water. Geophys. Res. Lett. 45, 11,247–11,256. https://doi.org/10.1029/2018GL080074.

Levy, R.H., Meyers, S.R., Naish, T.R., Golledge, N.R., McKay, R.M., Crampton, J.S., DeConto, R.M., De Santis, L., Florindo, F., Gasson, E.G.W., Harwood, D.M., Luyendyk, B.P., Powell, R.D., Clowes, C., Kulhanek, D.K., 2019. Antarctic ice-sheet sensitivity to obliquity forcing enhanced through ocean connections. Nat. Geosci. 12, 132–137.

Liebrand, D., De Bakker, A.T.M., Beddow, H.M., Wilson, P.A., Bohaty, S.M., Ruessink, G., Pälike, H., Batenburg, S.J., Hilgen, F.J., Hodell, D.A., Huck, C.E., Kroon, D., Raffi, I., Saes, M.J.M., van Dijk, A.E., Lourens, L., 2017. Evolution of the Early Antarctic Ice Ages. 114 (15). pp. 3867–3872. https://doi.org/10.1073/pnas.1615440114.

Liu, Y., Moore, J.C., Cheng, X., Gladstone, R.M., Bassis, J.N., Liu, H., Wen, J., Hui, F., 2015. Ocean-driven thinning enhances iceberg calving and retreat of Antarctic ice shelves. P. Natl. Acad. Sci. USA 112, 3263–3268. https://doi.org/10.1073/pnas.1415137112.

Lucchi, R.G., Rebesco, M., 2007. Glacial contourites on the Antarctic Peninsula margin: insights for palaeoenvironmental and paleoclimatic conditions. Geol. Soc. Spec. Publ. 276, 111–127. https://doi.org/10.1144/GSL.SP.2007.276.01.06.

Lyle, M., Gibbs, S., Moore, C., Rea, T.C., D.K., 2007. Late Oligocene Initiation of the Antarctic Circumpolar current: evidence from the South Pacific. Geology 35 (8), 691–694. https://doi.org/10.1130/G23806A.1.

Martin, E.E., Scher, H.D., 2004. Preservation of seawater Sr and Nd isotopes in fossil fish teeth: bad news and good news, Earth Planet. Sci. Lett. 220, 25–39.

Martin, E.E., Scher, H.D., 2006. A Nd isotopic study of southern sourced waters and Indonesian Throughflow at intermediate depths in the Cenozoic Indian Ocean, Geochemistry, Geophysics. Geosystems 7 (9). https://doi.org/10.1029/2006GC001302.

Martini, E., 1971. Standard Tertiary and Quaternary calcareous nannoplanktonzonation. In: Farinacci, A. (Ed.), Proceeding II Plankt. Conf., Roma, vol. 2,pp. 739–785.

Meredith, M., Sommerkorn, M., Cassotta, S., Derksen, C., Ekaykin, A., Hollowed, A., Kofinas, G., Mackintosh, A., Melbourne Thomas, J., Muelbert, M.M.C., Ottersen, G., Pritchard, H., Schuur, E.A.G., 2019. Polar Regions. In: IPCC Special Report on the Ocean and Cryosphere in a Changing Climate.

Moiroud, M., Pucéat, E., Donnadieu, Y., Bayon, G., Moriya, K., Deconinck, J.-F., Boyet, M., 2013. Evolution of the neodymium isotopic signature of neritic seawater on a northwestern Pacific margin: New constrains on possible end-members for the composition of deep-water masses in the late cretaceous ocean. Chem. Geol. 356, 160–170. https://doi.org/10.1016/j.chemgeo.2013.08.008.

Müller, R.D., Cannon, J., Qin, X., Watson, R.J., Gurnis, M., Williams, S., et al., 2018. GPlates: building a virtual Earth through deep time. Geochem. Geophys. Geosyst. 19. https://doi.org/10.1029/2018GC007584.

Naish, T.R., Wilson, G.S., Dunbar, G.B., Barrett, P.J., 2008. Constraining the amplitude of late Oligocene bathymetric changes in western Ross Sea during orbitally-induced oscillations in the East Antarctic Ice Sheet: (2) implications or global sea-level changes. Palaeogeogr. Palaeoclimatol. Palaeoecol. 260, 66–76. https://doi.org/10.1016/j.palaeo.2007.08.021.

Nakayama, Y., Menemenlis, D., Zhang, H., Schodlok, M., Rignot, E., 2018. Origin of Circumpolar Deep Water Intruding onto the Amundsen and Bellingshausen Sea Continental Shelves. Nat. Commun. 9 (1), 1–9. https://doi.org/10.1038/s41467-018-05813-1.

Nelson, C.S., Cooke, P.J., 2001. History of Oceanic Front Development in the New Zealand Sector of the Southern Ocean during the Cenozoic—a Synthesis. N. Z. J. Geol. Geophys. 44 (4), 535–553. https://doi.org/10.1080/00288306.2001.9514954.

Olbers, D., Borowski, D., Völker, C., Wölff, J., 2004. The dynamical balance, transport and circulation of the Antarctic Circumpolar current. Antarct. Sci. 16, 439–470.

Orsi, A.H., Whitworth, T., Nowlin, W.D., 1995. On the meridional extent and fronts of the Antarctic Circumpolar current. Deep-Sea Res. Pt. I 42, 641–673. https://doi.org/10.1016/0967-0637(95)00021-W.

Passchier, S., Ciarletta, D.J., Henao, V., Sekkas, V., 2018. Sedimentary processes and

facies on a high-latitude passive continental margin, Wilkes Land, East Antarctica. Geol. Soc. Lond., Spec. Publ. 475, 181–201. https://doi.org/10.6084/m9.figshare.c.4031218.v1.

Patterson, M.O., McKay, R., Naish, T., Escutia, C., Jimenez Espejo, F.J., Raymo, M.E., Meyers, S.R., Tauxe, L., Brinkhuis, H., Klaus, A., Fehr, A., Bendle, J.A.P., Bijl, P.K., Bohaty, S.M., Carr, S.A., Dunbar, R.B., Flores, J.A., Gonzalez, J.J., Hayden, T.G., Iwai, M., Katsuki, K., Kong, G.S., Nakai, M., Olney, M.P., Passschier, S., Pekar, S.F., Pross, J., Riesselman, C.R., Röhl, U., Sakai, T., Shrivastava, P.K., Stickley, C.E., Sugasaki, S., Tuo, S., van de Flierdt, T., Welsh, K., Williams, T., Yamane, M., 2014. Orbital forcing of the East Antarctic ice sheet during the Pliocene and Early Pleistocene. Nat. Geosci. 7, 841–847. https://doi.org/10.1038/ngeo2273.

Pekar, S.F., DeConto, R.M., Harwood, D.M., 2006. Resolving a late Oligocene conundrum: Deep-sea warming and Antarctic glaciation. Palaeogeogr. Palaeocl. 231, 29–40.

Pekar, S.F., Christie-Blick, N., 2008. Resolving Apparent Conflicts between Oceanographic and Antarctic Climate Records and Evidence for a Decrease in p CO 2 during the Oligocene through Early Miocene (34–16 Ma). 260. pp. 41–49. https://doi.org/10.1016/j.palaeo.2007.08.019.

Pfuhl, H.A., McCave, I.N., 2005. Evidence for late Oligocene Establishment of the Antarctic Circumpolar current. Earth Planet. Sci. Lett. 235 (3–4), 715–728. https://doi.org/10.1016/j.epsl.2005.04.025.

Piper, D.J.W., Brisco, C., 1975. Deep-water continental-margin sedimentation, dsdp Leg 28, Antarctica. In Hayes D.E., Frakes, L.A., et al., 1975 Initial Reports of the Deep Sea Drilling Project, Vol. 28, U.S. Government Printing Office, Washington pp.727–755. doi:https://doi.org/10.2973/dsdp.proc.28.121.1975.

Prebble, J., Crouch, E., Carter, L., Cortese, G., Bostock, H., Neil, H., 2013. An expanded modern dinoflagellate cyst dataset for the Southwest Pacific and Southern Hemisphere with environmental associations. Mar. Micropaleontol. 101, 33–48.

Pritchard, H.D., Ligtenberg, S.R.M., Fricker, H.A., Vaughan, D.G., Van Den Broeke, M.R., Padman, L., 2012. Antarctic Ice-Sheet Loss Driven by Basal Melting of Ice Shelves. Nature 484 (7395), 502–505. https://doi.org/10.1038/nature10968.

Rebesco, M., Hernández-Molina, F.J., Van Rooij, D., Wåhlin, A., 2014. Contourites and associated sediments controlled by deep-water circulation processes: State-of-theart and future considerations. Mar. Geol. 352, 111–154. https://doi.org/10.1016/j.margeo.2014.03.011.

Richey, J.N., Tierney, J.E., 2016. GDGT and alkenone flux in the northern Gulf of Mexico: Implications for the TEX86 and UK'37 paleothermometers. Paleoceanography 31 (12), 1547–1561.

Rignot, E., Mouginot, J., Scheuchl, B., van den Broeke, M., Van Wessem, M., Morlighem, M., 2019. Four decades of Antarctic Ice Sheet mass balance from 1979–2017.

Rintoul, S.R., 1998. On the origin and influence of Adélie Land Bottom Water. In Ocean, ice, and atmosphere: Interactions at the Antarctic continental margin (Vol. 75, pp. 151–171). Washington, DC: American Geophysical Union.

Rintoul, S.R., Hughes, C., Olbers, D., 2001. The Antarctic circumpolar current system. In: Siedler, G., Church, J., Gould, J. (Eds.), Ocean Circulation and Climate. Academic Press. Proc. Natl. Acad. Sci. USA, New York, pp. 271–302.

Rintoul, S.R., 2018. The global influence of localized dynamics in the Southern Ocean. Nature 558 (7709), 209–218. https://doi.org/10.1038/s41586-018-0182-3.

Rodriguez-Tovar, F.J., Dorador, J., 2014. Ichnological analysis of pleistocene sediments from the IODP Site U1385 "Shackleton Site" on the Iberian margin: approaching paleoenvironmental conditions. Palaeogeogr. Palaeoclimatol. Palaeoecol. 409, 24–32.

Rodríguez-Tovar, F.J., Nagy, J., Reolid, M., 2014. Palaeoenvironment of Eocene prodelta in Spitsbergen recorded by the trace fossil Phycosiphon incertum. Polar Res. 33, 23786.

Rodríguez-Tovar, F.J., Dorador, J., 2015. Ichnofabric characterization in cores: a method of digital image treatment. Ann. Soc. Geol. Pol. 85 (3), 465–471.

Rodríguez-Tovar, F.J., Dorador, J., Martin-Garcia, G.M., Sierro, F.J., Flores, J.A., Hodell, D.A., 2015a. Response of macrobenthic and foraminifer communities to changes in deep-sea environmental conditions from marine isotope stage (MIS) 12 to 11 at the "Shackleton Site" Glob. Planet. Chang. 133, 176–187.

Rodríguez-Tovar, F.J., Dorador, J., Grunert, P., Hodell, D., 2015b. Deep-sea trace fossil and benthic foraminiferal assemblages across glacial terminations 1, 2 and 4 at the "Shackleton Site" (IODP Expedition 339, Site U1385). Glob. Planet. Chang. 133, 359–370.

Rodríguez-Tovar, F.J., Dorador, J., Hodell, D.A.V., 2019. Trace fossils evidence of a complex history availability and oxygen conditions during Heinrich Event 1. Glob. Planet. Chang. 174, 26–34.

Salabarnada, A., Escutia, C., Röhl, U., Nelson, C.H., McKay, R., Jiménez-Espejo, F.J., Bijl, P.K., Hartman, J.D., Strother, S.L., Salzmann, U., Evangelinos, D., López-Quirós, A., Flores, J.A., Sangiorgi, F., Ikehara, M., Brinkhuis, H., 2018. Paleoceanography and ice sheet variability offshore Wilkes Land, Antarctica – part 1: Insights from late Oligocene astronomically paced contourite sedimentation, Clim. Past 14, 991–1014. https://doi.org/10.5194/cp-14-991-2018.

Sangiorgi, F., Bijl, P.K., Passchier, S., Salzmann, U., Schouten, S., McKay, R., Cody, R.D., Pross, J., Van De Flierdt, T., Bohaty, S.M., Levy, R., Williams, T., Escutia, C., Brinkhuis, H., 2018. Southern ocean warming and wilkes land ice sheet retreat during the mid-Miocene. Nat. Commun. 9, 317. https://doi.org/10.1038/s41467-017-02609-7.

Scher, H.D., Martin, E.E., 2004. Circulation in the Southern Ocean during the Paleogene inferred from neodymium isotopes. Earth Planet. Sci. Lett. 228, 391–405.

Scher, H.D., Bohaty, S.M., Zachos, J.C., Delaney, M.L., 2011. Two stepping into the ice-house: East Antarctic weathering during progressive ice-sheet expansion at the Eocene- Oligocene Transition. Geology 39, 383–386.

Schouten, S., Hopmans, E.C., Schefuß, E., Damste, J.S.S., 2002. Distributional variations in marine crenarchaeotal membrane lipids: a new tool for reconstructing ancient sea water temperatures? Earth Planet. Sci. Lett. 204 (1–2), 265–274.

Schouten, S., Hopmans, E.C., Rosell-Melé, A., Pearson, A., Adam, P., Bauersachs, T., Brocks, J.J., et al., 2013. An interlaboratory study of TEX86 and BIT analysis of sediments, extracts, and standard mixtures. Geochem. Geophys. Geosyst. 14 (12), 5263–5285.

Scotese, C.R., Wright, N., 2018. PALEOMAP Paleodigital Elevation Models (PaleoDEMS) for the Phanerozoic PALEOMAP Project, https://www.earthbyte.org/paleodem-resource-scotese-and-wright-2018.

Seki, A., Tada, R., Kurokawa, S., Murayama, M., 2019. High-resolution Quaternary record of marine organic carbon content in the hemipelagic sediments of the Japan Sea from bromine counts measured by XRF core scanner. Progress in Earth and Planetary Science 6 (1).

Seton, M., Müller, R.D., Zahirovic, S., Gaina, C., Torsvik, T.H., Shephard, G., Talsma, A., Gurnis, M., Turner, M., Maus, S., Chandler, M., July 2012. Global continental and ocean basin reconstructions since 200 Ma. Earth-Science Reviews 113 (3-4), 212–270. ISSN 00128252. https://doi.org/10.1016/j.earscirev.2012.03.002.

Shanmugam, G., Spalding, T.D., Rofheart, D.H., 1993. Traction structures in deep-marine, bottom-current-reworked sands in the Pliocene and Pleistocene, Gulf of Mexico. Geology 21, 929–932 10.1130/0091- 7613(1993)021 < 0929:TSIDMB > 2.3.CO;2.

Shaw, H., Wasserburg, G., 1985. Sm-Nd in marine carbonates and phosphates: Implications for Nd isotopes in seawater and crustal ages. Geochim. Cosmochim. Acta 49 (2), 503–518.

Sluijs, A., Pross, J., Brinkhuis, H., 2005. From greenhouse to icehouse; organic-walled dinoflagellate cysts as paleoenvironmental indicators in the Paleogene. Earth Sci. Rev. 68 (3–4), 281–315.

Sokolov, S., Rintoul, S.R., 2002. Structure of Southern Ocean fronts at 140°E. J. Mar. Syst. 37, 151–184. https://doi.org/10.1016/S0924-7963(02)00200-2.

Sokolov, S., Rintoul, S.R., 2009. Circumpolar structure and distribution of the Antarctiv Circumpolar current fronts: 1. Mean circumpolar paths. J. Geophysical Research 14. https://doi.org/10.1029/2008JC005108.

Sorlien, C.C., Luyendyk, B.P., Wilson, D.S., Bartek, L.R., Diebold, J.B., 2007. Oligocene development of the West Antarctic Ice Sheet recorded in eastern Ross Sea strata. Geology 35, 467–470.

Stow, D., Faugères, J.-C., 2008. Contourite Facies and the Facies Model, chap. 13. pp. 223–256.

Tachikawa, K., Athias, V., Jeandel, C., 2003. Neodymium budget in the modern ocean and paleo-oceanographic implications. Journal of Geophysical Research: Oceans (1978–2012) 108 (C8).

Tanaka, T., Togashi, S., Kamioka, H., Amakawa, H., Kagami, H., Hamamoto, T., Yuhara, M., Orihashi, Y., Yoneda, S., Shimizu, H., Kunimaru, T., Takahashi, K., Yanagi, T., Nakano, T., Fujimaki, H., Shinjo, R., Asahara, Y., Tanimizu, M., Dragusanu, C., 2000. JNdi-1: a neodymium isotopic reference in consistency with LaJolla neodymium. Chem. Geol. 168, 279–281.

Taylor, K.W., Huber, M., Hollis, C.J., Hernandez-Sanchez, M.T., Pancost, R.D., 2013. Re-evaluating modern and Palaeogene GDGT distributions: Implications for SST reconstructions. Glob. Planet. Chang. 108, 158–174.

Thompson, D.W.J., Solomon, S., 2002. Interpretation of recent Southern Hemisphere climate change. Science 296, 895–899.

Toggweiler, J.R., Russell, J., 2008. Ocean circulation in a warming climate. Nature 451, 286–288. https://doi.org/10.1038/nature06590.

van de Flierdt, T., Griffiths, A.M., Lambelet, M., Little, S.H., Stichel, T., Wilson, D., 2016. Neodymium in the oceans: a global database, a regional comparison and implications for palaeoceanographic research. Philos. Trans. R. Soc. A 374, 20150293.

van Wijk, E.M., Rintoul, S.R., 2014. Freshening drives contraction of Antarctic Bottom Water in the Australian Antarctic Basin. Geophys. Res. Lett. 41, 1657–1664. https://doi.org/10.1002/2013GL058921.

Weis, D., Kieffer, B., Maerschalk, C., Barling, J., de Jong, J., Williams, G.A., Hanano, D., Pretorius, W., Mattielli, N., Scoates, J.S., 2006. High-precision isotopic characterization of USGS reference materials by TIMS and MC-ICP-MS, Geochemistry, Geophysics. Geosystems 7 (8), Q08006.

Whitehead, J.M., Bohaty, S.M., 2003. Pliocene summer sea surface temperature reconstruction using silicoflagellates from Southern Ocean ODP Site 1165. Paleoceanography 18. https://doi.org/10.1029/2002PA000829.

Wilson, D.J., Piotrowski, A.M., Galy, A., Clegg, J.A., 2013. Reactivity of neodymium carriers in deep sea sediments: implications for boundary exchange and paleoceanography. Geochim. Cosmochim. Acta 109, 197–221. https://doi.org/10.1016/j.gca.2013.01.042.

Wright, N., Scher, H.D., Seton, M., Huck, C.E., Duggan, B.D., 2018. No Change in Southern Ocean Circulation in the Indian Ocean from the Eocene through late Oligocene' Paleoceanography and Paleoclimatology 33 (2), 152–167. https://doi.org/10.1002/2017PA003238.

Zachos, J., Pagani, M., Sloan, L., Thomas, E., Billups, K., 2001. Trends, rhythms, and aberrations in global climate 65 Ma to present. Science 292, 686–693.

Zhang, Y.G., Zhang, C.L., Liu, X.-L., Li, L., Hinrichs, K.-U., Noakes, J.E., 2011. Methane Index: A tetraether archaeal lipid biomarker indicator for detecting the instability of marine gas hydrates. Earth Planet. Sci. Lett. 307 (3–4), 525–534.

Zhang, Y.G., Pagani, M., Liu, Z., Bohaty, S.M., Deconto, R., 2013. A 40-million-year history of atmospheric CO2. Philos. T. R. Soc. A 371, 20130096. https://doi.org/10.1098/rsta.2013.0096.

Zhang, Y.G., Pagani, M., Wang, Z., 2016. Ring Index: A new strategy to evaluate the integrity of TEX86 paleothermometry. Paleoceanography 31 (2), 220–232.

Zonneveld, K.A., Marret, F., Versteegh, G.J., Bogus, K., Bonnet, S., Bouimetarhan, I., Crouch, E., de Vernal, A., Elshanawany, R., Edwards, L., Esper, O., Forke, S., Grøsfjeld, K., Henry, M., Holzwarth, U., Kielt, J.F., Kim, S.Y., Ladouceur, S., Ledu, D., Chen, L., Limoges, A., Londeix, L., Lu, S.H., Mahmoud, M.S., Marino, G., Matsouka, K., Matthiessen, J., Mildenhal, D., Mudie, P., Neil, H., Pospelova, V., Qi, Y., Radi, T., Richerol, T., Rochon, A., Sangiorgi, F., Solignac, S., Turon, J.L., Verleye, T., Wang, Y., Wang, Z., Young, M., 2013. Atlas of modern dinoflagellate cyst distribution based on 2405 data points. Rev. Palaeobot. Palynol. 191, 1–197. https://doi.org/10.1016/j.revpalbo.2012.08.003.